Data Assimilation for a Coupled Ocean-Atmosphere Model. Part I: Sequential State Estimation

Chaojiao Sun,[1] Zheng Hao,[2] Michael Ghil, and J. David Neelin

Department of Atmospheric Sciences

and Institute of Geophysics and Planetary Physics

University of California, Los Angeles

Revised version. Revised date: 2 July, 2001

[1] Corresponding author address: Dr. Chaojiao Sun, Hydrological Sciences Branch, NASA Goddard Space Flight Center, Mail Code 974, Greenbelt, MD 20771, USA. email: csun@hsb.gsfc.nasa.gov

[2]Now at: 3455 Rambow Dr., Palo Alto, CA 94306

Mon. Wea. Rev., sub judice

Short title: DATA ASSIMILATION FOR A COUPLED MODEL, I

Abstract

The assimilation problem for the coupled ocean-atmosphere system in the tropical Pacific is investigated using an advanced sequential estimator, the extended Kalman filter (EKF). The intermediate coupled model used in this study consists of an upper-ocean model and a steady-state atmospheric response to it. Model errors arise from the uncertainty in atmospheric wind stress. Data assimilation is applied in this idealized context to produce a time-continuous, dynamically consistent description of the model's El Niño/Southern Oscillation, based on incomplete and inaccurate observations. This study has two parts: Part I (the present paper) deals with state estimation for the coupled system, assuming that model parameters are correct, while Part II deals with simultaneous state and parameter estimation.

The dynamical structure of forecast errors is estimated sequentially using a linearized Kalman filter and compared with that of an uncoupled ocean model. The coupling produces large changes in the structure of the error-correlation field. For example, error correlations with opposite signs in the western and eastern part of the model basin are caused by wind-stress feedbacks.

The full EKF method is used to assimilate various model-generated synthetic oceanic data sets into the coupled model in an identical-twin framework. The assimilated data sets include the sea surface temperature and a combination of wave velocities and thermocline depth anomaly. With the EKF, the model's forecast-assimilation cycle is able to estimate correctly the phase and amplitude of the basic ENSO oscillation while using very few observations. This includes a set of observations that only cover a single meridional section of the ocean, preferably in the eastern basin.

1. Introduction and motivation

Interannual variability in the tropics is dominated by the El Niño/Southern Oscillation phenomenon (ENSO) (see Neelin *et al.*, 1998 for a review). Models of various degrees of complexity are capturing different aspects of interannual variability in the tropics with increasing success (see Latif *et al.*, 1998, for a review).

Consistence of the initial state with a coupled ocean-atmosphere model can result in smaller spin-up errors and useful forecast skill over longer lead times. Data assimilation with a fully coupled system is gaining therefore attention (Hao, 1994; Hao and Ghil, 1995). Recently, Chen *et al.* (1998, 1999) showed that the skill of the Lamont model (Cane *et al.*, 1986; Zebiak and Cane, 1987) can be considerably improved by assimilating better wind field data (NSCAT satellite-derived winds instead of Florida State University observed winds), as well as sea level data from Tropical Pacific tide gauges into the coupled model. Furthermore, to obtain a better initial state for an El Niño forecast, one should use all the observations available—from both ocean and atmosphere—especially those about the upper tropical ocean (Hao and Ghil, 1994; Miller *et al.*, 1995).

Here we present a data assimilation study with an intermediate coupled model using the extended Kalman filter (EKF). The main advantage of using the EKF is that it gives explicitly the evolution of forecast-error covariances, while the major difficulties in applying it are its computational cost and the need to specify the model-error covariance matrix $\mathbf{Q}$.

Recent progress in data assimilation for ocean models has been reviewed by Anderson *et al.* (1996). Cane *et al.* (1996) studied data assimilation using the Kalman filter via a reduced state space approach, to deal with the issues of computational cost and sparse data coverage. Fukumori *et al.* (1999) evaluated the feasibility and accuracy of assimilating satellite altimetry data into a global ocean general circulation model, using an approximate Kalman filter and smoother; following the approach of Fukumori and Malanotte-Rizzoli (1995), they computed the time-independent asymptotic limit of the forecast-error covariance $\mathbf{P}^{\mathrm{f}}$ on a reduced state space while carrying the model on the full grid. Verron *et al.* (1999) assimilated satellite data into a primitive-equation model with the EKF on a reduced state space. They found that this EKF was efficient in transferring the information from the surface-height observations to the deep ocean.

In this study, we compute the Kalman gain on the full space of the coupled model and conduct several "identical twin" experiments. Our intention here is to explore ENSO data assimilation using EKF on a simple enough yet fully coupled nonlinear model. By understanding the details of how EKF works and the way observational information is propagated in this intermediate coupled model, we hope to gain insight into the workings of the EKF when applied to more complicated models. In Part II of this paper we extend the approach to the problem of parameter estimation.

Studies like the present one that use synthetic data are worthwhile supplements to practically oriented studies with real data, in that the true-state history and model error statistics are known and can be compared easily with the results of the assimilation. Many studies have been carried out using real observations for *uncoupled* tropical-ocean models, as was the case in the past for atmospheric models (e.g., Ghil and Malanotte-Rizzoli, 1991). Some studies addressing ENSO have used real data, advanced data assimilation methods, and complete ocean models, but prescribed winds (e.g., Behringer *et al.*, 1998; Ngodock *et al.*, 2000; Verron *et al.*, 1999; Fukumori *et al.*, 1999). Simple data assimilation methodologies have been applied with intermediate coupled models to assimilate real data (e.g., Chen *et al.*, 1998, 1999).

Studies with advanced data assimilation systems and intermediate coupled models that have used real data, while valuable, are still at a fairly preliminary stage (Bennett *et al.*, 1998, 2000; Lee *et al.*, 2000). For example, Lee *et al.* (2000) used an adjoint method to assimilate monthly-mean data of sea-surface heights and temperatures, as well as wind stress, for September 1996 to January 1998. The method was applied to sliding six-month intervals of data, from September 1996 to July 1997, in an intermediate coupled model with a statistical diagnostic atmosphere component. Forecasts were issued from the last month of each such window and compared with the actual evolution of the system, based on assimilation results valid at the appropriate epoch. These authors found that the intermediate coupled model has a reasonable skill in reproducing observed interannual variability of SST and sea level during the 1997-98 El Niño.

In the present study, wind-stress error is considered to be the sole model deficiency. As the tropical oceans are largely wind-driven (Gill, 1980; Philander, 1990), errors in the wind stress have a great impact on the simulated ocean circulation (Leetma and Ji, 1989; Sheinbaum and Anderson, 1990; Fu *et al.*, 1993). Hao and Ghil (1994) and Miller *et al.* (1995) have shown that, in the absence of ocean-atmosphere feedback, oceanic data can compensate for errors in the wind stress. Even though an atmospheric component is included in a coupled ocean-atmosphere model, wind-stress error can still be present and produce large simulation errors, since higher-frequency variability dominates in the atmosphere than in the oceans. The profound effect of observed wind-stress errors on the prediction skill of a coupled model has been noticed by Graham *et al.* (1992).

We first present the dynamical structure of the forecast errors due to the wind-stress error in our coupled model, estimated with a linearized Kalman filter (LKF) scheme. The role of ocean-atmosphere coupling process in the propagation of model errors is investigated by comparing the results for the coupled case with those for the uncoupled one.

We then present the results of data assimilation using the extended Kalman filter (EKF). The most favorable places to measure the oceanic currents or sea surface temperature (SST) for recovering the ENSO cycle are examined by comparing the impact of assimilating observations at different longitudes.

Linear and nonlinear investigations of ENSO dynamics show that distinct parameter values can modify the coupled model's behavior, both quantitatively and qualitatively (Neelin *et al.*, 1998). One way to improve our model and its forecast skill is to estimate the correct value of its parameters from observations, at the same time as estimating the model state. This estimation is carried out with an extension of the EKF scheme, and relevant results are reported in Part II of this study.

The structure of the present paper (Part I of this study) is as follows: In section 2, we introduce the coupled ocean-atmosphere model used in the study. Further model details appear in Appendix A. In section 3, data assimilation methods are briefly reviewed, and two extensions of the Kalman filter to nonlinear problems, the LKF and EKF, are presented. The model-error covariance is constructed from wind-stress errors, with details presented in Appendix B. Section 4 contains the estimation of the forecast-error structure by the LKF experiments. Model-state estimation studies for the coupled model with the EKF and different data sources are reported in section 5. Concluding remarks appear in section 6.

2. Model solutions

We use the intermediate coupled model of Jin and Neelin (1993) and Neelin and Jin (1993) (jointly referred to as JN hereafter). The details of this coupled ocean-atmosphere model are described in Appendix A. This model is essentially a further idealization of the model of Zebiak and Cane (1987). The major simplification is to treat explicitly only the zonal dependence of sea surface temperature (SST) over an equatorial strip, with the meridional structure of the associated atmospheric forcing specified.

This coupled model presents two different kinds of ENSO oscillation, of the delayed-oscillator and westward-propagating type. The nature of the oscillation depends on the values of two key parameters, namely the relative coupling coefficient μ and the surface-layer coefficient δ_s (JN). In this study, we choose δ_s to be 0, and μ to be 0.76. These parameter values correspond to the delayed-oscillator regime of the model. The model parameters are given in Table 1. $\boxed{\text{Table 1}}$

The meridional structure of the mean currents in the upper layer of the ocean is projected onto the Hermite functions and truncated at a limited number (14 here). The coupled model thus boils down to a spatially one-dimensional system of evolution equations in the zonal direction x and time t. The amplitude for the Kelvin wave is q_0, while q_n for $n = 2, 4, ..., 14$ are the amplitudes of the first seven Rossby waves.

We use a staggered grid, with ocean wave coefficients $q_n, n = 0, 2, 4, ..., 14$, carried at full grid points, and SST carried at half grid points. The total length of the ocean basin is 150° (from 130°E to 80°W), with a grid spacing of 6.25°. The grid points in the x–direction are numbered from 1 to 25, going from the basin's western to its eastern boundary, and used in identifying the location of observing sections. The coupled system so discretized has

$(1+8)*24 = 216$ degrees of freedom. The time step is 6 hours (see Table 1).

To illustrate the impact of the ocean-to-atmosphere coupling feedback, an uncoupled ocean model otherwise similar to the coupled one is constructed. The former displays the same time evolution as the latter when starting from the same initial state and forced with the appropriate wind stress, recorded from the coupled control run. The wind stress used in the uncoupled case is no longer a function of the SST anomalies.

A 30-year run of the model confirms that it asymptotes rapidly to a limit cycle with a period of about 3.6 years (Fig. 1a). Figures 1b and 1c show the meridional structure of the SST anomalies at a transition phase (shortly after year 5) and a warm phase (near year 6), respectively. Figures 1d and 1e show the thermocline depth anomaly h at these two phases. It can be seen clearly that thermocline depth anomaly h leads SSTA. Hereafter, we will refer to the results of the model run without data assimilation (and without any errors imposed) as the "reference solution." The reference solution presents many typical features of the ENSO phenomenon, including a standing oscillation in SST, with subsurface dynamics providing the memory (Suarez and Schopf, 1988; Neelin *et al.*, 1994). Fig. 1

Figure 2 shows the time-longitude anomaly plots of the reference solution's SSTA, wind stress (τ), Kelvin-wave (q_0) and first Rossby-wave (q_2) amplitude for 30 years. The SST anomalies are confined to the eastern part of the basin. Their oscillation has a strong standing component, while slight eastward propagation is also present. The wind-stress anomalies lag slightly behind the SST anomalies in time, and are shifted to the west of the SST anomalies in space, with the maximum located in the central part of the basin. Figure 2

Differences in phase and in the location of the maxima among the SST, Kelvin- and Rossby-wave fields indicate the important effect of ocean-wave dynamics on the oscillation.

Notice that the slowly propagating oceanic weaves here are not the conventional free-basin modes, but rather a packet of mixed SST/ocean-dynamics modes of the coupled system (JN; Hao *et al.*, 1993; Neelin *et al.*, 1994). This is especially apparent in the presence of the Rossby-wave component along the equator itself, with opposite phases in the eastern and western part of the basin, while the Kelvin-wave component still exhibits predominantly eastward propagation.

Since the surface-layer coefficient δ_s is set to be zero here, the thermocline feedback dominates (JN; Hao *et al.*, 1993). Large variations of the SST in the eastern part of the basin are mainly due to the shallowness of the mean thermocline there. In the western part, the SST anomalies are smaller since the mean thermocline depth there is much greater.

3. Data assimilation methods

a. Methodology

1) EXTENDED KALMAN FILTER (EKF)

Since the SST equation is nonlinear, the extended Kalman filter (EKF) is applied here for assimilating the observations. In the EKF, the nonlinear model is linearized around the current state when estimating the propagation of the forecast error, while the state itself is advanced according to the full nonlinear model. Miller *et al.* (1994) discussed a number of distinct Kalman filter extensions to nonlinear systems. Ide and Ghil (1997a, b) studied the EKF for vortex systems in the time-continuous case. We describe the EKF here briefly, following the unified notation of Ide *et al.* (1997).

The model is given in discrete form by

$$\mathbf{x}^{\mathrm{f}}(t_{k+1}) = M_k[\mathbf{x}^{\mathrm{a}}(t_k)]. \tag{1}$$

Here $\mathbf{x}^{\mathrm{a}}(t_k)$ is the best estimate of the model state at the last time step k, and M_k is the state transition function; superscripts "a" and "f" stand for "analysis" and "forecast," respectively.

One assumes that the underlying natural system evolves according to the model (1), perturbed by random noise $\boldsymbol{\eta}(t_k)$,

$$\mathbf{x}^{\mathrm{t}}(t_{k+1}) = M_k[\mathbf{x}^{\mathrm{t}}(t_k)] + \boldsymbol{\eta}(t_k). \tag{2}$$

Here $\boldsymbol{\eta}$ is a Gaussian white-noise sequence, with mean zero and model-error covariance $\mathbf{Q}$, $E\boldsymbol{\eta}(t_k) = 0$ and $E\boldsymbol{\eta}(t_k)\boldsymbol{\eta}^{\mathrm{T}}(t_l) = \mathbf{Q}_k\delta_{kl}$, where E is the expectation operator and δ_{kl} is the Kronecker delta. The natural system's evolution is detected by observations contaminated by errors $\boldsymbol{\epsilon}_k^{\mathrm{o}}$,

$$\mathbf{y}_k^{\mathrm{o}} = H_k[\mathbf{x}^{\mathrm{t}}(t_k)] + \boldsymbol{\epsilon}_k^{\mathrm{o}}; \tag{3}$$

$\boldsymbol{\epsilon}_k^{\mathrm{o}}$ is also assumed to be Gaussian, white in time, with mean zero and covariance $\mathbf{R}_k$. The observation function H_k can be nonlinear as well. The superscripts "t" and "o" denote "truth" and "observation." Even though the dynamic model M_k and observation H_k may be nonlinear, a linear estimation of the model state, based on the observations, is sought:

$$\mathbf{x}^{\mathrm{a}}(t_k) = \mathbf{x}^{\mathrm{f}}(t_k) + \mathbf{K}_k\mathbf{d}_k, \tag{4}$$

where

$$\mathbf{d}_k = \mathbf{y}_k^{\mathrm{o}} - H_k[\mathbf{x}^{\mathrm{f}}(t_k)] \tag{5}$$

is the innovation vector. The weights $\mathbf{K}_k$ for the observations are obtained by minimizing the expectation of least-square distance between the analysis and the true state.

The EKF process can be divided into two steps (*e.g.* Gelb, 1974; Ghil and Malanotte-Rizzoli, 1991; Miller *et al.*, 1994) when observations are available at the current time t_k:

i) Forecasting step,

$$\mathbf{x}^{\mathrm{f}}(t_k) = M_{k-1}[\mathbf{x}^{\mathrm{a}}(t_{k-1})], \tag{6}$$

$$\mathbf{P}^{\mathrm{f}}(t_k) = \mathbf{M}_{k-1}\mathbf{P}^{\mathrm{a}}(t_{k-1})\mathbf{M}_{k-1}^{\mathrm{T}} + \mathbf{Q}(t_{k-1}); \tag{7}$$

ii) updating step,

$$\mathbf{x}^{\mathrm{a}}(t_k) = \mathbf{x}^{\mathrm{f}}(t_k) + \mathbf{K}_k\mathbf{d}_k, \tag{8}$$

$$\mathbf{P}^{\mathrm{a}}(t_k) = (\mathbf{I} - \mathbf{K}_k\mathbf{H}_k)\mathbf{P}^{\mathrm{f}}(t_k), \tag{9}$$

$$\mathbf{K}_k = \mathbf{P}^{\mathrm{f}}(t_k)\mathbf{H}_k^{\mathrm{T}}\left[\mathbf{H}_k\mathbf{P}^{\mathrm{f}}(t_k)\mathbf{H}_k^{\mathrm{T}} + \mathbf{R}_k\right]^{-1}. \tag{10}$$

The matrix $\mathbf{K}_k$ is the Kalman gain, which represents the optimal weight given to observations in updating the model state, and $\mathbf{H}_k$ is the linearized approximation of the observation function H_k. The state-transition matrix $\mathbf{M}_k$ is the state transition function M_k linearized about the current state. The system propagates the forecast-error covariance linearly in time, while the state itself evolves nonlinearly, with M_k. When the functions M_k and H_k are linear, the EKF reduces to the conventional Kalman filter. When there is no observation, only the forecasting step is performed, and the optimal estimation of the model state is the model forecast. The analysis-error covariance $\mathbf{P}_k^{\mathrm{a}}$ in this case is the same as the forecast-error covariance $\mathbf{P}_k^{\mathrm{f}}$.

2) LINEARIZED KALMAN FILTER (LKF)

The structure of the forecast-error covariance represents the impact of the model dynamics on the model-error propagation. For a nonlinear system, the evolution of the forecast-error covariances depends on the actual model trajectory. Given a prescribed trajectory, the propagation of model-error structure can be carried out independently, i.e., "off-line." When linearization is done along a prescribed trajectory, the resulting estimation process is called the linearized Kalman filter (LKF; Gelb, 1974; Fukumori and Malanotte-Rizzoli, 1995).

The LKF scheme, like the EKF, estimates the propagation of the model state and model error. The weights of the observations for the estimation of the model state are calculated according to (10). In the LKF scheme, however, the nonlinear functions H_k and M_k are linearized about the prescribed state vector $\mathbf{x}^{\mathrm{P}}$, which is specified prior to processing the observations. The Kalman gains may be precalculated and stored in the computer and there is no feedback of the updated model states on the estimation of $\mathbf{P}^{\mathrm{f}}$.

The LKF scheme is often used to avoid difficulties that arise from the need for repeated numerical differentiation of the state transition function M_k. Our main purpose in using it for the present study is to obtain as clear a picture as possible of the effects of coupling on the structure of the error correlation field.

On the other hand, the LKF is generally less successful in assimilating data than the EKF scheme because the fixed trajectory is often not as close to the true one as the sequentially updated trajectory (Gelb, 1974). Therefore, we implement the EKF scheme for the actual assimilation experiments with observations, but use the LKF scheme to investigate systematically and "off-line" model-error propagation in the absence of observations. In the present section, we use therefore Eq. (7) to compute the evolution of the error covariances, with the model matrix $\mathbf{M}_k$ given by the linearization of M_k about the reference solution of Fig. 1.

b. Error covariances

1) MODEL-ERROR COVARIANCE $\mathbf{Q}$

The most severe errors in tropical-ocean prediction seem to arise from wind-stress errors (Leetmaa and Ji, 1989; Graham *et al.*, 1992; Hao and Ghil, 1994; Miller *et al.*, 1995). We introduce, therefore, model errors at every time step by adding noise to the wind stress that is obtained from the model atmosphere's response to SST anomalies. The wind-stress error is specified as in Miller and Cane (1989), Miller *et al.* (1995) and Cane *et al.* (1996). It is taken as white in time and Gaussian-correlated and homogeneous in space. The errors are assumed to have the same meridional structure as the atmospheric response to the SST anomalies.

The particular form used for each component of the wind-stress error covariance matrix $\mathbf{Q}^{\mathrm{w}}$ is given by

$$< e_{k,i} e_{l,j} >= \sigma_\tau^2 \, \delta_{kl} \, e^{-(x_i - x_j)^2/2L_x^2}; \tag{11}$$

here $e_{k,i}$ and $e_{l,j}$ are the wind-stress errors at locations i and j, at time steps k and l, respectively, δ_{kl} is the Kronecker delta, σ_τ is the magnitude factor of the wind-stress error, and L_x the prescribed decorrelation distance. We use $\sigma_\tau = 0.02$ Pa and $L_x = 10°$ of longitude, as used by Miller and Cane (1989).

Model error is constructed by projecting the wind-stress error onto the prognostic model variables. The nonlinear SST equation (A1) is linearized with respect to the model's current state to obtain the model SST errors, i.e.,

$$\boldsymbol{\eta}(t_k) = \frac{\partial M_k}{\partial \tau} \mathbf{e}_k, \tag{12}$$

where τ is the wind stress and $\mathbf{e}_k$ is the wind-stress error at time t_k. Our model-error covariance $\mathbf{Q}$ is then computed from $\boldsymbol{\eta}$, as described in Appendix B.

Figure 3 shows model-error correlations between SST and selected ocean wave coefficients—the Kelvin (q_0), and the first and the last even Rossby coefficients of this model (q_2 and q_{14}). The autocorrelations of the model variables exhibit a structure similar to that of the wind-stress error imposed. All Rossby-wave modes are positively correlated with each other, since they travel in the same direction and thus the wind stress projects onto them with the same sign. However, model-error correlations between the Kelvin and Rossby waves are negative. Negative correlations among these waves were also obtained by Miller and Cane (1989), who considered the wind-stress noise in an equatorial ocean wave model. The SST correlates positively with the Kelvin and negatively with the Rossby waves. Figure 3

A first-order approximate projection, Eq. (B3), is used to transfer the model-error covariance of the wind stress to the model's other variables. Hence, the estimated forecast-error structure is accurate only when the model error is fairly small. A particular problem that may arise otherwise is loss of positive definiteness of $\mathbf{Q}$ during the projection procedure (Balgovind *et al.*, 1983; Parrish and Cohn, 1985; Boggs *et al.*, 1995; Gaspari and Cohn, 1999). The diagonal elements of $\mathbf{Q}$ are required here to be positive and have a minimum value on the order of 10^{-6} to prevent this problem from occurring. The assimilation experiment results shown later suggest that the projection, so modified, is satisfactory.

2) OBSERVATION-ERROR COVARIANCE $\mathbf{R}$

The observation error covariance matrix $\mathbf{R}$ is prescribed here as a diagonal matrix, $\mathbf{R}_{ij} = \sigma_i^2 \delta_{ij}$, where σ_i is the variance of the state variable x_i. The observations are represented as measurements T of SST, amplitudes q_n of the oceanic waves, or atmospheric wind-stress data τ at longitudinal locations; they are all taken twice a month if no other specification is given.

The observations are contaminated by white noise, with the following standard deviations: $\sigma_T^o = 0.5$ K; $\sigma_{q0}^o = 0.02$; $\sigma_{qn}^o = 0.01$; $\sigma_\tau^o = 0.01$ Pa. Note that the standard deviations for all wave coefficients are in nondimensional units. The equivalent observational errors for more conventional quantities—zonal current u, thermocline depth anomaly h, and vertical velocity w are: $\sigma_u^o = 0.02$ m s^{-1}; $\sigma_h^o = 1.2$ m; $\sigma_w^o = 0.275$ cm day^{-1}.

3) INITIAL FORECAST-ERROR COVARIANCE $\mathbf{P}_0^{\mathrm{f}}$

The initial errors are white in space, with the following standard deviations at all grid points: $\sigma_T = 0.9$ K; $\sigma_{q_0} = 0.06$; $\sigma_{q_n} = 0.04$, for $n = 2, 4, 6$; $\sigma_{q_n} = 0.03$, for $n = 8, 10, 12, 14$. The standard deviations for all wave coefficients are in nondimensional units, as for the observation errors. The initial forecast error covariance $\mathbf{P}_0^{\mathrm{f}}$ is assumed to have a diagonal structure, with its elements equal to the variances of the state variables at $t = 0$: $\mathbf{P}_{0ij}^{\mathrm{f}} = \sigma_i^2 \delta_{ij}$.

4. Forecast-error statistics

The behavior of forecast-error covariances is of interest for our understanding of how data assimilation works, in theory as well as in practice. For a linear system, the Kalman filter correctly estimates the forecast-error covariance, which represents the expected relationship between the forecast errors, based on initial uncertainties, model errors and model dynamics, and thus provides the optimal gain $\mathbf{K}$ for the observations. For a nonlinear system, the EKF is nearly optimal in most circumstances (but not all; see the discussion of Miller *et al.*, 1994, 1999, for various strongly nonlinear models). In this section, we study forecast-error propagation by linearized model dynamics according to (7), in preparation for the actual data assimilation experiments.

The random wind-stress errors affect the evolution of $\mathbf{P}^{\mathrm{f}}$ by appearing in (7) through the model-error covariance $\mathbf{Q}$. The latter is obtained according to the error model governed by (11) and (12). In practice, we have used a different value of $\mathbf{Q}_k$ at each time step k. This value was obtained by using the Kronecker product $\mathbf{Q}_k = \boldsymbol{\eta}_k \boldsymbol{\eta}_k^{\mathrm{T}}$, without averaging, with each $\boldsymbol{\eta}_k$ being a particular random vector. The time-averaged effect on the evolution of $\mathbf{P}_k^{\mathrm{f}}$ is approximately the same as using an average $\mathbf{Q}$, given by Eq. (B7), for each time step.

a. Uncoupled case

Experiments are carried out first for the uncoupled case. In this case, the tropical ocean model includes no ocean-atmosphere coupling feedback and is forced by a prescribed time sequence of wind-stress, generated by the coupled model. With no wind-stress noise added, the uncoupled run reproduces the time evolution of the ocean in the reference solution.

The state transition function M_k can be written symbolically as

$$M_k = M_k^{(o)} \oplus M_k^{(a)} \oplus M_k^{(c)}. \tag{13}$$

Here $M_k^{(o)}$ represents the ocean operator, given by Eqs. (A1)–(A19); $M_k^{(a)}$ the atmospheric operator, given by the linear Eq. (A20); and $M_k^{(c)}$ the coupling operator, given by Eqs. (A21)–(A28). The symbolic summation operation $\oplus$ indicates that the set of variables on which one of the nonlinear operators on the right-hand side of Eq. (13) acts, differs from the other two sets and that together these three sets of variables span the entire state space of the full model. The linearized version of (13) is then

$$\mathbf{M}_k = \mathbf{M}_k^{(o)} \oplus \mathbf{M}_k^{(a)} \oplus \mathbf{M}_k^{(c)}. \tag{14}$$

For the forecast-error evolution in the uncoupled case we thus use

$$\mathbf{M}_k = \mathbf{M}_k^{(o)} \tag{15}$$

with prescribed wind stress. The LKF in this case still uses the full $\mathbf{Q}_k$, as described above. This is not entirely self-consistent but helps us isolate and highlight further the role of coupled vs. uncoupled dynamics in forecast-error evolution.

To track the error evolution, we compute the estimation error standard deviation, i.e., the square root of each diagonal entry of $\mathbf{P}^{\mathrm{f}}$, and refer to it as the root-mean-square (RMS) error hereafter. In the uncoupled case, the RMS error of each field at each grid point reaches an asymptotic behavior after a fairly short transient of a few months. This asymptotic behavior is the result of the competition between three effects: (i) the oscillatory dynamics of the model ; (ii) the steady pumping of error into the model by the addition of $\mathbf{Q}_k$ at every step k; and (iii) numerical dissipation that mimics physical dissipation of energy and, hence, error (Ghil *et al.*, 1981; Fukumori and Malanotte-Rizzoli, 1995).

In the uncoupled model, with no feedback between ocean and atmosphere, the forecast errors for the amplitude q_0 of the Kelvin wave and q_2 of the first Rossby wave quickly reach their steady-state levels (Figs. 4b, c). This saturation is expected since the ocean is driven by the wind and no SST changes are allowed to feed back to the oceanic waves in this case. Thus the latter two effects balance each other almost exactly and the oscillatory effect is absent from the wave-component errors. At steady state, the Kelvin wave exhibits a fairly gradual eastward increase of the forecast error, while the Rossby waves have almost constant forecast error over most of the basin, with larger values concentrated near the eastern basin boundary. Figs. 4

SST forecast errors, on the other hand, are dominated by a regular oscillation with a period of about 3.6 years, as suggested by Fig. 1 (see also Jiang *et al.*, 1995; Moron *et al.*, 1998). They are concentrated overall in the central and eastern basin, while their peak values lie in the central basin (Fig. 4a). At the time where these peak values reach their asymptotic steady state, at $t \simeq 15$ years, they are about twice as large as the accumulated model errors directly imposed on the SST field (not shown). This difference indicates that the wind-stress error transmitted through the oceanic waves to the SST is amplified by the model dynamics; but the RMS errors in SST also reach a cyclo-stationary steady state, due to the balance between the model-error pumping and the dissipation.

The zonal variations of the forecast errors for the ocean waves are consistent with the analytical arguments by Miller and Cane (1989) that the faster Kelvin wave picks up more wind-stress errors on its way eastward, while the slower Rossby waves do not accumulate much error during their propagation westward, since the wind-stress error is white in time, but correlated spatially. The large Rossby-wave forecast errors that occur at the eastern boundary are due to the reflection of the Kelvin wave, which has a larger forecast-error level there (Fig. 4c).

The forecast-error correlations estimated by LKF at the end of 5 years are shown in Fig. 5, by which time a fairly steady structure has emerged. The correlation patterns display clearly the impact of the oceanic waves: the autocorrelations for Kelvin or Rossby waves are broadened in their respective directions of propagation (Figs. 5d and 5g). The angle between the axis of maximum positive correlation of distinct Rossby waves and the main diagonal—about 22° for q_2 and q_4 vs. 39° between q_2 and q_{14} (see Figs. 5h and 5i)—is related to the difference between their wave speeds; e.g., q_4 travels at 3/7 of the speed of q_2, while q_{14} travels at 1/9 of q_2's speed. The positive correlations near either zonal boundary between the Kelvin and Rossby waves (Figs. 5e, f) stem from the wave reflection there. The slower phase speed of the highest wave (q_{14}) results in a much smaller positive region for its correlation

Fig. 5

with the Kelvin wave (Fig. 5f) than that in the cross-correlation between the lowest Rossby wave q_2 and the Kelvin wave q_0 (Fig. 5e).

The ocean's thermodynamic processes result in a tight SST autocorrelation for the western part of basin, and broader structure in the central and eastern basin (Fig. 5a). The wide correlation area is associated with the large SST forecast error in the eastern basin (Fig. 4a). The positive correlation between the SST and Kelvin wave is consistent with the oceanic waves' impact in the finite basin on the SST: the Kelvin wave anomalies excited by the wind stress in the central basin induce SST changes with the same sign on the way to the east, while Rossby waves reflected from the Kelvin wave off the eastern boundary also enhance the SST changes in the eastern basin (Figs. 5b and 5c). However, the Rossby waves directly excited by the wind stress and their Kelvin-wave reflection off the western basin boundary correlate negatively with the SST changes in the entire basin (Fig. 5c). These negative correlations represent the negative feedback process between the ocean and atmosphere there.

b. Coupled case

The LKF is applied next to the coupled model to estimate its forecast-error structure. The model-error covariances $\mathbf{Q}_k$ are the same as for the uncoupled case, while the linearized error-evolution dynamics is now given by the full $\mathbf{M}_k$ of Eq. (14). The difference between the coupled and uncoupled cases is in the state transition matrix $\mathbf{M}$.

The forecast errors in the coupled case are much larger than those in the uncoupled case (Fig. 6). The expected forecast errors in SST anomalies (Fig. 6a) are one order of magnitude larger than in the uncoupled case, but the spatio-temporal pattern of the errors Fig. 6

is quite similar (cf. Fig. 4a). The coupling processes clearly amplify the model's SST errors. The errors in the oceanic wave amplitudes q_0 and q_2 (Figs. 6b, c) are a few times larger than in the uncoupled case (see Figs. 4b, c) and their patterns differ substantially from the uncoupled case. In the latter, both q_0 and q_2 errors were steady in time after 5 years and increased monotonically from west to east, gradually for q_0 and abruptly near the eastern boundary for q_2 (Figs. 4b, c). In the coupled case at hand, both q_0 and q_2 evolve over the first ten years toward a fairly regular oscillation, with two separate maxima, in the eastern and western basin (Figs. 6b, c). For the Kelvin wave, the maximum in the eastern basin is larger, while it is larger in the western basin for the first Rossby wave. This makes sense given the accumulation of errors as each wave propagates across the basin.

The forecast-error correlation structure of the coupled case, estimated by LKF at the end of year 5, is shown in Fig. 7. The forecast-error correlations in the coupled and the uncoupled cases have, overall, similar structures when SST is involved (compare Figs. 7a–c with Figs. 5a–c). Roughly speaking, the SST errors over the entire basin are negatively correlated with the errors in the oceanic waves over the western part of the basin and positively correlated over the eastern part. The relatively small differences between these correlations and those in the uncoupled case are not surprising, because the model-parameter values used in the present paper—moderate coupling of $\mu = 0.76$ and no upwelling feedback, i.e. $\delta_s = 0$—yield a strong influence of thermocline depth on SST.

Fig. 7

The forecast-error statistics of the oceanic waves, on the other hand (Figs. 7d–i), show major differences between the coupled and uncoupled cases. The coupling processes enhance all the correlations, especially the cross-correlations between oceanic waves, and emphasize an East-West seesaw pattern. This seesaw structure is expressed by negative auto- as well as cross-correlations of the ocean waves in the western basin, and might be related to the most unstable coupled mode in this intermediate model (JN; see also Figs. 6b, c).

5. Assimilation experiments

With confidence in our sequential estimation approach confirmed in the previous section on covariance propagation, we continue the investigation by assimilating various types of observations. The questions which we want to address in this "model world" campaign are: What is the minimum number of observations needed in order to follow the evolution of an ENSO cycle? Where should these observations best be taken to minimize estimation error for the ocean state and SST?

We conduct identical-twin experiments in which the true model history, as well as the forecast and observations, are produced by the same model. The true history differs from the reference solution in Figs. 1 and 2 in two respects: (i) an initial error that is drawn from the distribution having $\mathbf{P}_0^{\mathrm{f}}$ as its covariance matrix; and (ii) model errors drawn from a distribution that has $\mathbf{Q}_k$ as its covariance matrix and are imposed at each step during the model simulation. The observations are taken twice a month and differ from the true-state history due to errors in the observation process with covariance matrix $\mathbf{R}$. The matrices $\mathbf{P}_0^{\mathrm{f}}$, $\mathbf{Q}$ and $\mathbf{R}$ were all described in section 3b.

The assimilation experiments are all carried out for 30 years. They start from an initial state that differs from the true initial state by having a different phase along the reference solution's limit cycle. In these experiments, we use the full EKF, according to Eqs. (6)–(10). The case of a model that generates the true-state history being different from the one that is used for the assimilation is handled in Part II.

In the following experiments, q_n data at a single point refer to observations of all the oceanic waves included in the model at that zonal location. Since the meridional structure of the ocean fields is projected on the Hermite functions, these observations are equivalent to having measured mass and velocity fields for a whole meridional section: the projection operator is bijective (1-to-1 and onto) when restricted to the finite-dimensional subspace of interest. In reality, oceanic observations do not provide direct measurements of q_n. However, in our present, highly simplified model, q_n data can be used directly and should provide theoretical guidance on how to use subsurface mass and velocity data in a coupled system.

a. Simulated true state

Figure 8 shows the time evolution of the SST anomalies, wind-stress τ, Kelvin-wave amplitude q_0 and the first Rossby-wave amplitude q_2 for the simulated true-state history that starts with perturbed initial data. In our terminology, the *reference solution* (see Fig. 2) is the model run without any errors imposed, while the history of the *true states* is generated by adding errors to the initial state and to the wind-stress forcing. The wave fields q_0 and q_2 are noisier than the SST anomalies because the wave coefficients q_n, $n = 0, 2, ..., 14$, are directly affected by the wind-stress noise while SST is only influenced through the integrated effect of the wind errors [see Eq. (A20)]. Figure 8

We choose the initial state of the true-state history to be in a different phase of the ENSO cycle than the reference solution's initial state. The reference solution (see Fig. 2a) starts from a transient phase that enters immediately a cold-anomaly phase (La Niña), while the true-state history (see Fig. 8a) starts from the next transient phase that enters immediately a warm-anomaly phase (El Niño). Our data assimilation experiments all start out with the model's initial state being the same as in the reference solution (Fig. 2a), rather than the "true" initial state (Fig. 8a).

b. State estimation

1) SST DATA AT A SINGLE LOCATION

We first perform an EKF assimilation run with a single SST observation located in the eastern basin at 108°W. To the extent that the SST equation (A1) in the JN model represents off-equatorial behavior as well, such an SST observation should also be thought of as a meridional section of SST measurements.

Time evolution of the SST anomaly and the amplitude q_0 of the Kelvin wave over 30 years are presented in Figs. 9a, b. EKF assimilation does recover the phase information of the true-state history with the initial state starting from a different phase (compare Fig. 9a with Fig. 8a). The diagonal elements of the forecast-error covariance matrix $\mathbf{P}^{\mathrm{f}}$ (dashed) and analysis error covariance matrix $\mathbf{P}^{\mathrm{a}}$ (solid) for the SST (Fig. 9c) are concentrated in the eastern basin, while those of q_0 are spread over the whole basin (Fig. 9d). This is not surprising because we have seen in sections 4a and 4b that SST forecast errors are the largest in the central and eastern basin, while the forecast errors for the wave amplitudes q_n are large across the whole basin (see especially Fig. 6). The improvements in both SST and q_0 indicate that the SST information is transferred to the oceanic waves by the EKF assimilation. That the latter does capture the ocean-atmosphere coupling processes well is consistent with the large SST–ocean-wave cross-correlations in Fig. 7. Figs. 9

We wish to determine the preferred observing location for the SST, so that the forecast errors are smallest when the unique SST observation is taken at that location. To do so, EKF experiments were performed for two other SST observation locations, in the western basin at 152°E and in the central basin at 177°W. The three single-SST experiments will be referred to by the index of the grid point at which the single observation is taken. It is found that the assimilation errors for SST observations are smallest when using the SST data in the eastern basin (Fig. 9), and increase when the SST observation moves toward the west.

The RMS errors of the EKF assimilation across the basin width are shown in Fig. 10 for the model forecast without data assimilation, as well as for the three experiments with SST data located in the eastern, central and western basin. The state-estimation errors when using an SST observation in the eastern basin at 108°W (denoted by SST_{20}) for the SST anomaly, Kelvin and the first two Rossby-wave amplitudes (heavy solid) are consistently quite small. Their being less than 10% of the maximal model-forecast errors (short dashes) indicates the effectiveness of the EKF scheme. Fig. 10

The assimilation errors with the single observation at 177°W (denoted by SST_9) are considerably larger, but still less than 50% of the maximal errors. The data assimilation experiment using an SST observation in the western basin at 152°E (denoted by SST_4) barely reduces the model forecast errors without data assimilation (short dashes). The latter assimilation experiment fails to recover the right phase of the true-state history, even though it recovers the correct magnitude of the anomalies (not shown). This is not surprising because in our simple coupled model, there is not much SST signal in the western basin at all (see Figs. 2a and 8a).

The results in Figs. 9 and 10 suggest that the single-section SST measurements in the eastern part of the basin are most valuable, those in the central basin are still quite useful but do not reduce the estimation errors as much as necessary, while those in the western basin are barely useful at all. The usefulness of SST data can be related to the corresponding forecast error at the observed location, since the SST errors are largest in the eastern part of the basin and decreased westward (Fig. 10a). In fact, roughly speaking, the contribution of an observation in an EKF-based assimilation is proportional to the corresponding forecast-error variance at the observed location; see Eqs. (4) and (10).

2) SUBSURFACE DATA AT A SINGLE LOCATION

The EKF assimilation of the subsurface data q_n at a single location in the eastern basin (111°W) works as well as that of the SST data nearby and even somewhat better (Figs. 11a, c). Note that we assumed all the ocean-wave coefficients q_n, $n = 0, 2, ..., 14$, are known at that location. The analysis-error covariances $\mathbf{P}^{\mathrm{a}}$ (solid) are successfully reduced by the q_n updates and result in forecast-error covariances $\mathbf{P}^{\mathrm{f}}$ (dashed) that are barely any larger (Figs. 11b, d). Alternate odd and even peaks in $\mathbf{P}^{\mathrm{f}}$ for SST (Fig. 11c) correspond to positive and negative phases of the SST anomaly cycle (Fig. 8a). Figs. 11

The forecast-error correlations estimated by EKF at the end of 10 years are shown in Fig. 12. Compared to the LKF estimates for the coupled model (Fig. 7), the autocorrelations (Figs. 12a, d, g vs. 7a, d, g) are quite similar but the cross-correlations differ more noticeably. The latter differences are probably due to the fact that the EKF captures better than the LKF the evolution in the spatial error structure over a full ENSO cycle. Perhaps most telling is the difference in the structure of the cross-correlations between SST and q_0 (Fig. 12b vs. 7b). The EKF must be capturing the nonlinearity in the subsurface temperature relation to thermocline depth that in turn affects SST. This relation is known to differ between a warm and a cold phase. Fig. 12

The preferred location to measure subsurface data is investigated by using ocean-wave data q_n at a single location in the western (149°E), central (180°) or eastern basin (111°W). The improvements in the SST (Fig. 13a) and ocean-wave fields (Figs. 13b–d) are very similar. Fig. 13 This is to be expected because the forecast errors in Kelvin- and Rossby-wave amplitudes are comparable in different parts of the ocean basin (see Figs. 6b, c). Since strong ocean-wave signals are present throughout the basin (see Figs. 2b, d and 8b, d), q_n observations taken at different locations are able to provide the information needed to recover the true state.

Uncoupled ocean-wave propagation is the mechanism of ENSO memory in the delayed-oscillator "toy models" for ENSO (Suarez and Schopf, 1988; Battisti and Hirst, 1989; Jin, 1997; Burgers, 1999). If this were the case in less highly idealized models, one might think that observations in the western part of the basin would provide the most useful information. Hao and Ghil (1994) showed this to be true for the uncoupled ocean model of Cane and Patten (1984), which is slightly more realistic than the JN ocean model used here. They attributed this result in their model to the Kelvin waves' greater speed and hence efficiency in carrying information eastward.

The same could be true in the coupled situation, if the wind-stress forcing were perfectly simulated by the model. Because the coupled model is imperfect, however, the western-basin observational information—carried eastward, albeit quite efficiently, by Kelvin waves—becomes less accurate than the data observed in the eastern basin (Figs. 13b–d). Hence the q_n data from the central and eastern basin are just as useful in our coupled model as those from the western basin.

3) THREE SST OBSERVATIONS

Additional assimilation experiments were carried out in which a number of distinct sections of SST and q_n data were used. These are included in Table 2, along with the results Table 2 of the single-section experiments already discussed. We show 30-year RMS values of Niño-3 SST, and those of ocean-wave coefficients q_0, q_2 and q_4 averaged over the whole basin.

An EKF experiment with SST observations at three locations—177°W, 139°W, and 108°W—is denoted by "3∗SST" in Table 2. The errors in this case are much smaller than when using SST data in the west-central basin (177°W) only, but just slightly better than those with SST data in the east-central basin (139°W) or the eastern basin (108°W) alone. The small gain by using the additional SST data over a single, well-placed cross-section suggests that the latter can deliver most of the benefits, at least in this simple model.

4)MULTIPLE SUBSURFACE SECTIONS

We saw that a single section of subsurface data gives assimilation results that are better than the best single-section results with SST data. The ocean-wave results are almost independent of the single section's location, as the corresponding curves in Fig. 14 are almost indistinguishable. The numerical results in Table 2 show that, in fact, the farther east the section the better, albeit by a very small margin.

To see whether one can still improve, in our simple coupled model, the EKF results for subsurface data, we ran assimilation experiments with multiple q_n sections. We denote the case with two observations of q_n at 149°E and 111°W as the "$2{*}q_n$" case, and the case with observations of q_n at 5 locations—at 143°E, 160°E, 180, 142°W, and 111°W—as the "$5{*}q_n$" case (Table 2).

The assimilation run with five sections does have the smallest errors overall, in both SST and Rossby waves, but the additional gains of using the $2{*}q_n$ and $5{*}q_n$ data sets over the eastern-basin data at 111°W only are quite limited. In fact, the Kelvin-wave error in the $5{*}q_n$ experiment is slightly worse than in other experiments with subsurface data, and both the q_0 and q_2 errors are slightly worse than in the q_{n20} experiment. These are subtle effects due to the model's distinct dispersion relation for the Kelvin vs. the Rossby waves and its nonlinearity. We refer to Hao and Ghil (1994) for a discussion of the effect of wave dispersion on data assimilation in a linear, two-dimensional shallow-water model of the tropical Pacific and to Miller *et al.* (1994) for a similar discussion of the effect of nonlinearities in zero-dimensional but highly nonlinear models.

Such subtleties aside, one cross-section of subsurface data appears rather satisfactory for this simple coupled model. Better spatial resolution and a more faithful representation of both oceanic and atmospheric processes could, however, increase the number of degrees of freedom that are active in the system and thus the number of observations required to track it accurately.

c. Weights assigned by EKF

To understand how the EKF treats the data in different parts of the basin, the weights given to the observations in the two-section set of subsurface data are examined in Fig. 14. Fig. 14

The weights shown here are snapshots at time step $t = 1, 2, ..., 30$ years.

The observations in the eastern part of the basin are given much more weight overall, in particular when the affected variable is distinct from the observed one (see especially Figs. 14a and d). Since the strongest interaction between the SST and wave fields occurs in the eastern basin, it is reasonable to assign a larger weight to oceanic observations there, given the same observational accuracy, especially when correcting SST. This emphasis on eastern-basin observations is smaller when considering the effect of q_0 or q_2 on each other (Figs. 14c and e). Note that the weights given to either q_0 or q_2 when updating the field that is being observed (Figs. 14b and f)—at the observation location itself—is about 0.5. This confirms that our assimilation scheme is well-balanced, in the sense that it assigns comparable weights to the current observations, on the one hand, and to the forecast based on past observations, on the other.

We also find that the weights have similar shapes and magnitudes during different phases of ENSO, except for the weights given to q_2 observations when updating SST (Fig. 14d). The shapes are still similar in the warm and cold phases, but the magnitude of the weights and the locations where the weights peak are shifted. During the warm phase, the q_n observations in the eastern basin (q_{n20}: black curves) are given larger weights in updating SST, and the largest weight occurs further towards the basin's east coast than during the cold phase, while the observations in the western basin (q_{n4}: gray curves) are given smaller weights. During the cold phase, the observations in the western basin are given more weight and the maximum of the weights—for both q_{n4} and q_{n20} observations—occurs further towards the central basin. The magnitude of the weights during the transitions phases of ENSO are in-between the extreme-phase magnitudes. The EKF thus assimilates observations of oceanic waves in the eastern basin more effectively during El Niño, while the observations in the central basin are more useful during La Niña.

6. Conclusions

a. Summary

In this paper, we studied data assimilation for a simple, but fully coupled tropical ocean-atmosphere model. Our coupled model is based on Jin and Neelin's (1993) and Neelin and Jin's (1993) (JN throughout the main text) "stripped-down" version of Zebiak and

Cane's (1987) model and consists of an upper-ocean model of the tropical Pacific and a steady-state atmospheric response to the ocean model's SST anomalies. An advanced data assimilation method, the extended Kalman filter (EKF), was used to tackle the model's nonlinearity. This coupled model is simple enough for the EKF to be applied to its full state space and can serve therefore as a benchmark for future data assimilation studies with more realistic and highly resolved coupled models.

Wind-stress errors were assumed to be the sole source of model errors. This assumption is a useful simplification for two complementary reasons. First, wind-stress errors are a dominant source of errors in the estimation and prediction of the tropical climate system (Miller and Cane, 1989; Hao and Ghil, 1994; Chen *et al.*, 1999). Second, wind-stress errors represent schematically the main effects of weather noise in the system.

We started by investigating the dynamical structure of the forecast errors in either the coupled or uncoupled framework, by applying the linearized Kalman filter (LKF), which propagates the error's covariance matrix linearly along a reference solution (Fig. 2). The forecast-error structure for the coupled model differs from that of the uncoupled one. The ocean-atmosphere coupling feedback enhances the forecast-error correlations, especially the cross-correlations among the various oceanic waves (compare Figs. 5 and 7).

The coupling induces and reinforces, in particular, a seesaw feature along the equator, with error correlations of opposite sign in the oceanic waves on either side of the ocean basin. This seesaw pattern seems to result from the constraint imposed on the waves by the tropical ocean's Sverdrup balance between the surface forcing and the pressure gradient. The influence of wave reflection at the zonal boundaries is also enhanced in the coupled case. The difference between the forecast-error covariances of the uncoupled and coupled cases thus suggests that we pay special attention in passing from data assimilation in the former to the latter.

Next, we have shown that the EKF scheme can effectively estimate the tropical ocean-atmosphere state for the coupled model. To restore the phase and amplitude of its ENSO oscillation, the model needs only observations covering a single meridional section. Either sea-surface temperature (SST) or subsurface data along such a section appear to suffice (Figs. 9 and 11).

The location of SST observations should be well chosen: a section located in the eastern basin tends to be the most useful (Fig. 10 and Table 2). The usefulness of SST observations decreases towards the western part of the basin. Subsurface data anywhere in the basin reduce the initial errors dramatically (Fig. 13), with the section in the eastern basin having the smallest errors (Table 2). The nonlocal response of the atmosphere to the SST anomalies ensures a smooth wind field and hence ocean-wave fields that are smooth, too. Atmospheric observations of the wind stress, which is not a prognostic variable of the model, can be easily assimilated with the EKF scheme as well (not shown here).

b. Discussion

The EKF extracts the information content of sparse observations, greatly enhancing the usefulness of a limited data set. The small number of data needed to track the coupled model's periodic solution in the present model is probably due to the fact that a pair of oscillatory modes with a simple spatial structure dominate its evolution. This fact was demonstrated for the model at hand by JN and Hao *et al.* (1993).

The dominance of a few simple modes in the temporally irregular and spatially rich behavior of a number of related ENSO models was shown by Jin *et al.* (1994, 1996) and Tziperman *et al.* (1994), among others. Rasmusson (1991), Keppene and Ghil (1992), Jiang *et al.* (1995) and other authors also found a large fraction of the observed variance in the tropical Pacific's various climatic fields to be captured by a few oscillatory modes. Ghil and Jiang (1998) showed that predicting the, possibly related, quasi-biennial and low-frequency mode is crucial for the accuracy of both dynamical and statistical ENSO forecasts. Ghil and Robertson (2000) argued, therefore, that the evidence from a full hierarchy of climate models, up to and including general circulation models (GCMs)—as well as from observations and real-time forecast skill—supports the dominance of a few oscillatory modes in ENSO variability on seasonal-to-interannual scales.

This situation for the tropical coupled system resembles that encountered for the mid-latitude ocean or atmosphere: a very small number of data can suffice to track solutions of idealized models thereof (Todling and Ghil, 1994; Ghil and Todling, 1996; Ide and Ghil, 1997a, b). Ghil (1997), in reviewing this work, concluded that the number of data required to track a model solution with the EKF can be comparable to the number of the model's dominant, linearly unstable and nonlinearly equilibrated modes (see also Ghil and Ide, 1994, and Dee, 1995).

Indeed, our work, as well as other data assimilation studies for the tropical Pacific that rely on the Kalman filter (Cane *et al.*, 1995, 1996) and the EKF (Verron *et al.*, 1999) suggest that the number of observations needed can be as small as the number of degrees-of-freedom required to describe the system's evolution over the time interval of observation. As we require to describe accurately a larger fraction of the variance, the number of modes required to capture that fraction increases, and a larger number of observations will be needed. This number can still be much smaller than the model's number of grid-point or spectral-coefficient variables, even for much more highly resolved and realistic models. Similar arguments apply to the size of a Monte Carlo ensemble required for the accurate and efficient performance of an ensemble Kalman filter (see also Keppene, 2000; Mitchell and Houtekamer, 2000).

The forecast experiments carried out in Part II of our study using simulated data from a Tropical Ocean-Global Atmosphere (TOGA)–Tropical Atmosphere Ocean (TAO)–like array assimilated into the model's oceanic component suggest that once a relatively large set of observations is available, initialization of the uncoupled ocean model might suffice for good coupled forecasts, given the atmosphere's rapid adjustment to the ocean state. Still, further improvements of the ENSO forecasts can be made by using the coupled model in the assimilation process. It is shown in Part II that the "TOGA-TAO" data are sufficient for good forecast skill in this intermediate model, and can be expected to provide accurate enough initial states for a more complete coupled model, when using the EKF.

The next step toward an advanced forecast-and-analysis cycle in a fully coupled GCM is to examine EKF or slightly suboptimal filter performance (Todling and Cohn, 1994; Ghil, 1997) in a somewhat more realistic coupled ocean-atmosphere model. Such a model could still have an oceanic component like the one used here. It would include, however, a prognostic atmospheric component, albeit a fairly simple one. For a coupled system with both components of GCM complexity, however, it is not clear how close to optimality a feasible data assimilation scheme can be. The requirement to assimilate the fairly sparse observations currently available into such a complex model, which has very different dominant time scales in its oceanic and atmospheric components, points to the need for advanced assimilation technology that yields initial fields consistent with the forecast dynamics.

Acknowledgments. This work has evolved from ZH's doctoral work. It was supported by NASA grants NAG-5317 (MG and ZH) and NAG 5-9294 (MG and CS), and NOAA grant NA86GP0314 (JDN) at UCLA and by a UCAR fellowship for the IRICP Pilot Project at UCSD (ZH). CS wishes to thank K. Ide for stimulating discussions and helpful suggestions, and R. N. Miller for the help with the mathematical procedure to generate white noise with a prescribed covariance. MG also wishes to acknowledge the sabbatical hospitality of the Laboratoire de Météorologie Dynamique du CNRS, Ecole Normale Supérieure, Paris, and the support of a Visiting Chair of the French Académie des Sciences. Computational resources were provided mainly by the Department of Atmospheric Sciences, UCLA, the San Diego Supercomputer Center, and the Supercomputer Center of Florida State University.

Appendix A. The model

The model description here is brief and we refer the reader to Jin and Neelin (1993) for details. The feedback between the ocean and atmosphere takes place every time step.

a. The ocean

The ocean dynamics is described by linear shallow-water equations for the currents and a nonlinear equation for the sea-surface temperature (SST). The dynamical variables are the three velocity components, (u, v, w), and the thermocline depth anomaly h. We list and explain the parameter values in Table 1.

1) SST EQUATION

The equation for the SST in the equatorial band is

$$\frac{\partial T}{\partial t} + u_1 \frac{\partial T}{\partial x} + \mathcal{H}(w) \frac{w}{H_{1.5}}(T - T_{sub}) - \mathcal{H}(-v_N) \frac{2v_N}{L_y}(T - T_N) + \epsilon_T (T - T_0) = 0 \tag{A1}$$

where T is the temperature of the surface mixed layer, u_1 the zonal current in this surface layer, w the vertical surface current, and v_N the meridional surface current at the northern boundary of the equatorial box. Symmetry of SST and antisymmetry of v_N are assumed.

The equilibrium value T_0 of SST is set at 29°, $\epsilon_T = (90 \text{ days})^{-1}$ is the Newtonian damping time, L_y is the width of the box, and T_N is the off-equatorial SST at a distance L_y from the equator. The depths H_1 and H_2 of the two layers are taken here to be 50 m and 100 m, while $H_{1.5} = 75$ m is the depth scale that characterizes upwelling of the subsurface temperature T_{sub}.

An analytical, smooth version $\mathcal{H}(x)$ of the Heaviside function $H(x)$ is used here,

$$H(x) = \begin{cases} 1 & x > 0, \\ 0 & x \le 0; \end{cases} \tag{A2}$$

see Eq. (B6) in the next appendix.

The meridional velocity v_N can be obtained by finite differencing of the continuity equation:

$$2\frac{v_N}{L_y} = \frac{w}{H_1} - \frac{\partial u_1}{\partial x} \tag{A3}$$

The subsurface temperature T_{sub} is parameterized as a function of thermocline depth anomaly h—a deeper thermocline is associated with warmer upwelled waters:

$$T_{sub} = T_{s0} + (T_0 - T_{s0}) \tanh\,(\frac{h + h_0}{h_*}) \tag{A4}$$

2) OCEAN CURRENTS

The vertical-mean motions above the thermocline are governed by the linearized reduced-gravity shallow-water equations on a β-plane in the long-wave approximation,

$$\delta\frac{\partial u}{\partial t} - \beta y v + \epsilon u = -g\frac{\partial h}{\partial x} + \frac{\tau}{\rho H}, \tag{A5}$$

$$\beta y u = -g\frac{\partial h}{\partial y}, \tag{A6}$$

$$\delta\frac{\partial h}{\partial t} + H(\frac{\partial u}{\partial x} + \frac{\partial v}{\partial y}) + \epsilon h = 0. \tag{A7}$$

Here τ is the zonal wind stress, ρ is the oceanic density, $H = H_1 + H_2$ is the total depth of the two layers, and $\epsilon = (2.5\text{yr})^{-1}$ is the damping rate for the vertical-mean current. The relative adjustment time coefficient δ measures the ratio of the time scale of adjustment by oceanic dynamics to the net time scale of SST change through the SST equation.

The usual boundary conditions for the shallow-water equations in the long-wave approximation are used

$$u = 0 \quad \text{at} \quad x = x_E, \tag{A8}$$

$$\int_{\infty}^{-\infty} u dy = 0 \quad \text{at} \quad x = x_W, \tag{A9}$$

where x_E and x_W locate the eastern and western boundaries, respectively.

Given the linear change of variables

$$q = h + u, \tag{A10}$$

$$r = h - u, \tag{A11}$$

the shallow-water equations (A5)–(A7) can be rewritten with q, r, and v as the dependent variables, in nondimensional units. Following JN, we truncate the equations so obtained to include only the Kelvin mode and the first seven symmetric Rossby modes. The resulting equations for the oceanic wave coefficients q_n are

$$(\delta\frac{\partial}{\partial t} + \epsilon)q_0 + \frac{\partial q_0}{\partial x} = \tau_0, \tag{A12}$$

$$(n-1)(\delta\frac{\partial}{\partial t} + \epsilon)q_n - \frac{\partial q_n}{\partial x} = n\tau_n - [(n-1)]^{1/2}\tau_{n-2}, n = 2, 4, ..., 14; \tag{A13}$$

here τ_n is the zonal wind stress projected onto oceanic mode n, q_0 is the amplitude of the Kelvin wave, and q_n, $n = 2, 4, ..., 14$, are the amplitudes of the first seven Rossby waves.

The horizontal components u_s and v_s of the vertical-shear current are governed by steady-state equations dominated by damping due to interfacial stress between the layers (Zebiak and Cane, 1987):

$$\epsilon_s u_s - \beta y v_s = \frac{\tau H_2}{\rho H_1 H}, \tag{A14}$$

$$\epsilon_s v_s + \beta y u_s = 0, \tag{A15}$$

where $\epsilon_s = (2\ \text{days})^{-1}$ is the damping coefficient for the shear currents.

The vertical component w_s of the shear currents can be calculated from the continuity equation using u_s and v_s:

$$w_s = H_1(\frac{\partial u_s}{\partial x} + \frac{\partial v_s}{\partial y}). \tag{A16}$$

For simplicity, the three components of the shear current are written as:

$$u_s = b_u \tau, \tag{A17}$$

$$v_s = -\frac{L_y}{2H_1} b_w \frac{\tau}{\rho H}, \tag{A18}$$

$$w_s = -b_w \tau + H_1 b_u \frac{\partial \tau}{\partial x}; \tag{A19}$$

here $b_u \approx H_2/H_1\epsilon_s$ and $b_w \approx (H_1/L_d)b_u$, and L_d is the characteristic meridional length scale determined by the damping time scale of vertical mixing: $L_d \equiv \epsilon_s/\beta$.

b. The atmosphere

The steady response of the zonal wind-stress anomalies τ' to SST anomalies T' at the equator is

$$\tau'(x,0) = \mu A[\frac{3}{2} e^{3\epsilon_a x} \int_x^{x_E} T'(s) e^{-3\epsilon_a s} ds - \frac{1}{2} e^{\epsilon_a s} \int_{x_W}^{x} T'(s) e^{\epsilon_a s} ds]. \tag{A20}$$

Here A is an amplitude factor, ϵ_a is a Rayleigh friction due to boundary-layer turbulence, and μ is an ocean-atmosphere coupling parameter.

c. Climatological state and coupling

A smooth function that resembles the mean-annual observed wind stress in the Pacific along the equator is used to set up the basic state:

$$\overline{\tau} = 0.60\{0.12 - \cos^2[(x - x_0)\frac{\pi}{2x_0}]\}, \tag{A21}$$

with $x_0 = 0.57L$, where L is the basin width.

The coupled system is set up using one-way flux correction (Neelin, 1990), with total wind stress τ given by

$$\tau = \overline{\tau} + \tau'; \tag{A22}$$

τ' is derived from the atmospheric response to SST anomalies T',

$$T' = T - \overline{T}, \tag{A23}$$

according to Eq. (A20).

It is convenient to introduce a relative surface-layer coefficient δ_s which controls the anomalous surface-layer currents due to coupling. These currents can thus be reduced or even turned off completely to examine their effects without affecting the climatology:

$$u_s = \overline{u}_s, \tag{A24}$$

$$v_s = \overline{v}_s + \delta_s v'_s, \tag{A25}$$

$$w_s = \overline{w}_s + \delta_s w'_s. \tag{A26}$$

Here $\overline{u}_s, \overline{v}_s, \overline{w}_s$ are the velocity components associated with the climatological wind stress, while u'_s, v'_s, w'_s are shear currents associated with the coupling:

$$w'_s = -b_w \tau' + H_1 b_u \frac{\partial \tau'}{\partial x}, \tag{A27}$$

$$v'_s = -b_w \tau'. \tag{A28}$$

Note that for the data assimilation experiments here, u_s does not depend on δ_s.

Appendix B. The model-error covariance Q

The model-error covariance **Q** is derived from the wind-stress errors. Since the SST eqation (A1) is nonlinear, linearization along the updated trajectory is employed when projecting the wind-stress error. Schematically, our coupled system can be written in discrete form as

$$T_k^f = z(T_{k-1}^a, q_{k-1}^a) + g(T_{k-1}^a, q_{k-1}^a, \tau_{k-1}^a + e_{k-1}^a), \tag{B1}$$

$$q_k^f = L_q(q_{k-1}^a) + L_\tau(\tau_{k-1}^a + e_{k-1}^a); \tag{B2}$$

here q_k represents the state vector for all the q_n, $n = 0, 2, ..., 14$, at time step k, and e_k is the wind-stress error at k. Since the oceanic waves have simple linear dynamics, $L_\tau(\cdot)$ and $L_q(\cdot)$ are linear operators, while $z(\cdot,\cdot)$ and $g(\cdot,\cdot,\cdot)$ are nonlinear functions associated with the advection terms in the SST equation.

Because of the interaction of the model state with the random noise e_k in the wind stress, function g is very rough and cannot be integrated in the traditional Riemann or even Lekesgue sense. Of the two forms of calculus available for stochastic processes, we use the Stratonovich calculus here. Unlike the often-used Itô calculus, it resembles the traditional calculus in allowing the chain rule for differentiation (e.g., Penland, 1996).

The linearized coupled system is

$$T_k^f \approx z(T_{k-1}^a, q_{k-1}^a) + g(T_{k-1}^a, q_{k-1}^a, \tau_{k-1}^a) + \frac{\partial g(T_{k-1}^a, q_{k-1}^a, \tau_{k-1}^a)}{\partial \tau} e_{k-1}, \tag{B3}$$

$$q_k^f = L_q(q_{k-1}^a) + L_\tau(\tau_{k-1}^a) + L_\tau(e_{k-1}^a). \tag{B4}$$

The model SST errors η_i^T in Eq. (12) at grid point i (and time step k) are then computed from the wind-stress errors e_i and e_{i+1} (both at time step k), at grid points i and $i+1$, according to

$$\begin{aligned} \frac{\eta_i^T}{\Delta t} &= -\frac{b_u}{2\Delta x}[(1-\delta_{i,1})(T_i - T_{i-1})e_i + (1-\delta_{i,N-1})(T_{i+1} - T_i)e_{i+1}] \\ &\quad - \frac{1}{H_{1.5}}[\frac{1}{w_0}\mathcal{H}'(\frac{w_i}{w_0}) + \mathcal{H}(\frac{w_i}{w_0})](T_i - T_{isub})[-b_w(e_i + e_{i+1}) + \frac{H_1 b_u}{\Delta x}(e_{i+1} - e_i)] \\ &\quad - \frac{b_w}{H_1}[-\frac{1}{v_0}\mathcal{H}'(\frac{v_i}{v_0})] + \mathcal{H}(\frac{v_i}{v_0})](T_i - T_N)(e_{i+1} + e_i); \end{aligned} \tag{B5}$$

here b_u and b_w are the coefficients associated with the shear currents, as in Eqs. (A17–A19), while Δt and Δx are the time step and grid spacing, respectively. Note that we choose a smooth function $\mathcal{H}(x)$ to represent the Heaviside function $H(x)$ of Eq. (A2),

$$\mathcal{H}(x) = \frac{1}{2}[1 + tanh(x)]; \tag{B6}$$

in (B5), w_0 and v_0 are appropriate scaling factors for the respective arguments of $\mathcal{H}$.

The model-error covariance $\mathbf{Q}$ is finally computed as

$$\mathbf{Q} = < \boldsymbol{\eta}\boldsymbol{\eta}^{\mathrm{T}} >, \tag{B7}$$

where $\boldsymbol{\eta}^{\mathrm{T}}$ is the transpose of the vector $\boldsymbol{\eta}$.

References

Anderson, D. L. T., J. Sheinbaum, and K. Haines, 1996: Data assimilation in ocean models. *Rep. Prog. Phys.* , **59**, 1209–1266.

Balgovind, R., A. Dalcher, M. Ghil, and E. Kalnay, 1983: A stochastic-dynamic model for the spatial structure of forecast error statistics. *Mon. Wea. Rev.*, **115**, 273–296.

Battisti, D. S., and Hirst, A. C., 1989: Interannual variability in the tropical atmosphere/ocean system: influence of the basic state and ocean geometry. *J. Atmos. Sci.*, **45**, 1687–1712.

Behringer, D. W., M. Ji, and A. Leetmaa, 1998: An improved coupled model for ENSO prediction and implications for ocean initialization. Part I: The ocean data assimilation System. *Mon. Wea. Rev.*, **126**, 1013–1021.

Bennett, A.F., B.S. Chua, D. E. Harrison, and M. J. McPhaden, 1998: Generalized inversion of Tropical Atmosphere-Ocean data and a coupled model of the tropical Pacific. *J. Climate*, **11**, 1768–1792.

Bennett, A.F., B.S. Chua, D. E. Harrison, and M. J. McPhaden, 2000: Generalized inversion of Tropical Atmosphere-Ocean (TAO) data and a coupled model of the tropical Pacific. Part II: The 1995-96 La Niña and 1997-98 El Niño. *J. Climate*, **13**, 2,770–2,785.

Boggs, D., M. Ghil, and C. Keppenne, 1995: A stabilized sparse-matrix U-D square-root implementation of a large-state extended Kalman filter. *Proc. WMO 2nd International Symposium on Assimilation of Observations in Meteorology and Oceanography, Tokyo, March 1995*, WMO/TD-No 651, World Meteorological Organization, 219–224.

Burgers, G., 1999: The El Niño stochastic oscillator. *Clim. Dyn.*, **15**, 521–531.

Cane, M. A. and R. J. Patton, 1984: Numerical model for low-frequency equatorial dynamics. *J. Phys. Oceanogr.*, **14**, 1853–1863.

Cane, M. A., S. E. Zebiak, and S. C. Dolan, 1986: Experimental forecasts of El Nino. *Nature*, **321**, 827–832.

Cane, M. A., S. E. Zebiak, and Y. Xue, 1995: Model studies of the long-term behavior of ENSO. In National Research Council (D. G. Martinson *et al.*, Eds.), *Natural Climate Variability on Decade-to-Century Time Scales*, National Academy Press, 442–457.

Cane, M. A., A. Kaplan, R. N. Miller, B. Tang, E. C. Hackert, and A. J. Busalacchi, 1996: Mapping tropical Pacific sea level: Data assimilation *via* a reduced state space Kalman filter. *J. Geophys. Res.*, **101**, 22,599–22,617.

Chen, D., M. A. Cane, S. E. Zebiak, and A. Kaplan, 1998: The impact of sea level data assimilation on the Lamont model prediction of the 1997/98 El Niño. *Geophys. Res. Lett.*, **25**, 2837–2840.

Chen, D., M. A. Cane, and S. E. Zebiak, 1999: The impact of NSCAT winds on predicting the 1997/98 El Niño: A case study with the Lamont-Doherty Earth Observatory model. *J. Geophys. Res.*, **104**, 11,321–11,327.

Dee, D. P., 1995: On-line estimation of error variance parameters for atmospheric data assimilation. *Mon. Wea. Rev.*, **123**, 1128–1145.

Evensen, G., 1994: Sequential data assimilation with a nonlinear quasi-geostrophic model using Monte Carlo methods to forecast error statistics. *J. Geophys. Res.*, **99**, 10143–10162.

Fu, L.-L., I. Fukumori, and R. N. Miller, 1993: Fitting dynamic models to the Geosat sea level observations in the tropical Pacific ocean. Part II: A linear, wind-driven model. *J. Phys. Oceanogr.*, **23**, 2162–2181.

Fukumori, I., and P. Malanotte-Rizzoli, 1995: An approximate Kalman filter for ocean data assimilation: An example with an idealized Gulf Stream model. *J. Geophys. Res.*, **100**, 6777–6793.

Fukumori, I., R. Raghunath, L.–L. Fu, and Y. Chao, 1999: Assimilation of TOPEX/Poseidon altimeter data into a global ocean circulation model: How good are the results? *J. Geophys.*

Res., **104**, 25,647–25,665.

Gaspari, G., and S. E. Cohn, 1999: Construction of correlation functions in two and three dimensions. *Quart. J. Roy. Meteor. Soc.*, **125**, 723–757.

Gelb, A. (Ed.), 1974: *Applied Optimal Estimation.* The MIT Press, Cambridge, Mass., 374 pp.

Ghil, M., 1997: Advances in sequential estimation for atmospheric and oceanic flows. *J. Met. Soc. Japan*, **75**, 289–304.

Ghil, M., and P. Malanotte-Rizzoli, 1991: Data assimilation in meteorology and oceanography. *Adv. Geophys.*, **33**, 141–266.

Ghil, M., and K. Ide, 1994: Extended Kalman filtering for vortex systems: An example of observing-system design. Data Assimilation: A New Tool for Modeling the Ocean in a Global Change Perspective, P. Brasseur and J. C. H. Nihoul (Eds.), Springer-Verlag, 167–191.

Ghil, M., and R. Todling, 1996: Tracking atmospheric instabilities with the Kalman filter, Part II: Two-layer Results. *Mon. Wea. Rev.*, **124**, 2340–2352.

Ghil, M., and N. Jiang, 1998: Recent forecast skill for the El Niño/Southern Oscillation. *Geophys. Res. Lett.*, **25**, 171–174.

Ghil, M., and A. W. Robertson, 2000: Solving problems with GCMs: General circulation models and their role in the climate modeling hierarchy. *General Circulation Model Development: Past, Present and Future*, D. Randall (Ed.), Academic Press, San Diego, pp 285-325.

Gill, A. E., 1980: Some simple solutions for heat induced tropical circulation. *Quart. J. Roy. Meteor. Soc.*, **106**, 447–462.

Graham, N. E., T. P. Barnett, and M. Latif, 1992: Considerations of the predictability of ENSO with a lower-order coupled model. *TOGA Notes*, **7**, 11–15.

Hao, Z., 1994: *Data Assimilation for Interannual Climate-Change Prediction.* Ph.D. Dissertation, Dept. of Atmospheric Sciences, University of California, Los Angeles, CA 90095, 223 pp.

Hao, Z., and M. Ghil, 1994: Data assimilation in a simple tropical ocean model with wind-stress errors. *J. Phys. Oceanogr.*, **24**, 2111–2128.

Hao, Z. and M. Ghil, 1995: Sequential parameter estimation for a coupled ocean-atmosphere model. *Proc. WMO 2nd International Symposium on Assimilation of Observations in Meteorology and oceanography, Tokyo, March 1995*, WMO/TD-No. 651, World Meteorological Organization. 181–186.

Hao, Z., J. D. Neelin, and F.-F. Jin, 1993: Nonlinear tropical air-sea interaction in the fastwave limit. *J. Climate*, **6**, 1523–1544.

Ide, K., and M. Ghil, 1997a: Extended Kalman filtering for vortex systems. Part I: Methodology and point vortices. *Dyn. Atmos. Oceans*, **27**, 301–332.

Ide, K., and M. Ghil, 1997b: Extended Kalman filtering for vortex systems. Part II: Rankine vortices and observing-system design. *Dyn. Atmos. Oceans*, **27**, 333–350.

Ide, K., P. Courtier, M. Ghil, and A. C. Lorenc, 1997: Unified notation for data assimilation: Operational, sequential and variational. *J. Met. Soc. Japan*,**75**, 181–189.

Jiang, N., J.D. Neelin, and M. Ghil, 1995: Quasi-quadrennial and quasi-biennial variability in COADS equatorial Pacific sea surface temperature and winds. *Clim. Dyn.*, **12**, 101–112.

Jin, F.-F. , 1997: An equatorial ocean recharge paradigm for ENSO. Part I: conceptual model. *J. Atmos. Sci.*, **54**: 811–829.

Jin, F.-F. , and J. D. Neelin, 1993: Modes of interannual tropical ocean-atmosphere interaction—a unified view. Part I: Numerical Results. *J. Atmos. Sci.*, **50**, 3478–3503.

Jin, F.-f., J. D. Neelin and M. Ghil, 1994: El Niño on the Devil's Staircase: Annual subharmonic steps to chaos, *Science*, **264**, 70–72.

Jin, F.-F., J. D. Neelin, and M. Ghil, 1996: El Niño/Southern Oscillation and the annual cycle: Subharmonic frequency-locking and aperiodicity. *Physica D*, **98**, 442–465.

Keppenne, C.L., 2000: Data assimilation into a primitive-equation model with a parallel ensemble Kalman filter. *Mon. Wea. Rev.*, **128**, 1971–1981.

Keppenne, C. L., and M. Ghil, 1992: Adaptive filtering and prediction of the Southern Oscillation index. *J. Geophys. Res.*, **18**, 20449–20454.

Latif, M., D. Anderson, T. Barnett, M. Cane, R. Kleeman, A. Leetmaa, J. O'Brien, A. Rosati, and E. Schneider, 1998: A review of the predictability and prediction of ENSO. *J. Geophys. Res.*, **103**, 14,375–14,393.

Lee, T., J.-P. Boulanger, A. Foo, L.-L. Fu, and R. Giering, 2000: Data assimilation by an intermediate coupled ocean-atmosphere model: Application to the 1997-1998 El Niño. *J. Geophys. Res.*, **105**, 26,063–26,087.

Leetmaa, A., and M. Ji, 1989: Operational hindcasting of the tropical Pacific. *Dyn. Atmos. Oceans*, **13**, 465–490.

Miller, R. N., and M. A. Cane, 1989: A Kalman filter analysis of sea level height in the tropical Pacific. *J. Phys. Oceanogr.*, **19**, 773–790.

Miller, R. N., M. Ghil, and F. Gauthiez, 1994: Advanced data assimilation in strongly nonlinear dynamical systems. *J. Atmos. Sci.*, **51**, 1037–1056.

Miller, R. N., A. J. Busalacchi, and E. C. Hackert, 1995: Sea surface topography fields of the tropical Pacific from data assimilation. *J. Geophys. Res.*, **100**, 13389–13425.

Miller, R. N., E. F. Carter Jr., and S. T. Blue, 1999: Data assimilation into nonlinear stochastic models. *Tellus*, **51A**, 167–194.

Mitchell, H. L., and P. L. Houtekamer, 2000: An adaptive ensemble Kalman filter. *Mon. Wea. Rev.*, **128**, 416–433.

Moron, V., R. Vautard, and M. Ghil, 1998: Trends, interdecadal and interannual oscillations in global sea-surface temperatures. *Clim. Dyn.*, **14**, 545–569.

Neelin, J. D., 1990: A hybrid coupled general circulation model for El Niño studies. *J. Atmos. Sci.*, **47**, 674–693.

Neelin, J. D., and F.-F. Jin, 1993: Modes of interannual tropical ocean-atmosphere interactoin—a unified view. Part II: Analytical results in the weak-coupling limit. *J. atmos. Sci.*, **50**, 3504–3522.

Neelin, J. D., M. Latif, and F.-F. Jin, 1994: Dynamics of coupled ocean-atmosphere models: The tropical problem. *Annu. Rev. Fluid Mech.*, **26**, 617–659.

Neelin, J. D., D. S. Battisti, A. C. Hirst, F.-F. Jin, Y. Wakata, T. Yamagata, and S. E. Zebiak, 1998: ENSO theory. *J. Geophys. Res.*, **103**, 14261–14290.

Ngodock, H. E., B. S. Chua, and A. F. Bennett, 2000: Generalized inverse of a reduced gravity primitive equation ocean model and tropical atmosphere-ocean data. *Mon. Wea. Rev.*, **128**, 1,757–1,777.

Parrish, D. F., and S. E. Cohn, 1985: A Kalman filter for a two-dimensional shallow water model: formulation and preliminary experiments. *Office Note 304*, National Meteorological Center, Washington DC 20233, 64 pp.

Penland, C., 1996: A stochastic model of IndoPacific sea surface temperature anomalies. *Physica D*, **98**, 534–558.

Philander, S. G., 1990: *El Niño, La Niña, and the Southern Oscillation.* Academic Press, 293 pp.

Rasmusson, E. M., X. Wang and C. F. Ropelewski, 1990: The biennial component of ENSO variability. *J. Marine Syst.*, **1**, 71–96.

Sheinbaum, J., and D. L. T. Anderson, 1990: Variational assimilation of XBT data. Part II. Sensitivity studies and use of smoothing constraints. *J. Phys. Oceanogr.*, **10**, 689–704.

Suarez, M. J., and P. S. Schopf, 1988: A delayed action oscillator for ENSO, *J. Atmos. Sci.*, **45**, 3283–3287.

Todling, R., and S. E. Cohn, 1994: Suboptimal schemes for atmospheric data assimilation based on the Kalman filter. *Mon. Wea. Rev.*, **122**, 2530–2557.

Todling, R., and M. Ghil, 1994: Tracking atmospheric instabilities with the Kalman filtering. Part I: Methodology and one-layer results. *Mon. Wea. Rev.*, **122**, 183–204.

Tziperman, E., L. Stone, M.A. Cane, and H. Jarosh, 1994: El Niño chaos: overlapping of resonances between the seasonal cycle and the Pacific ocean-atmosphere oscillator. *Sciences*, **264**, 72–74.

Verron, J., L. Gourdeau, D. T. Pham, R. Murtugudde, and A. J. Busalacchi, 1999: An extended Kalman filter to assimilate satellite altimeter data into a nonlinear numerical model of the tropical Pacific Ocean: Method and validation. *J. Geophys. Res.*, **104**, 5441–5458.

Zebiak, S. E., and M. A. Cane, 1987: A model El Niño Southern Oscillation. *Mon. Wea. Rev*,, **115**, 2262–2278.

Chaojiao Sun, Goddard Earth Sciences and Technology Center, University of Maryland Baltimore County, and Hydrological Sciences Branch, NASA Goddard Space Flight Center, Greenbelt, MD 20771.

Michael Ghil, J. David Neelin, Department of Atmospheric Sciences, University of California, Los Angeles, 405 Hilgard Ave., CA 90095-1565

Zheng Hao, 3455 Rambow Dr., Palo Alto, CA 94306

Received RECEIPT DATE; revised REVISION DATE; accepted ACCEPT DATE.

Figure Captions

Figure 1. Reference solution for 30 years: (a) Niño-3 SST (solid; the dashed line denotes the mean); (b) SST anomaly field (labeled SSTA) and (d) thermocline depth anomaly field h at the transition phase shortly after year 5; (c) and (e) SSTA and h at the warm phase around year 6. The symbol $*$ denotes the time of the two phases, for which the SSTA and h are plotted. Note that SSTA is zero outside the equatorial strip by definition.

Figure 2. Longitude-time plots (Hovmöler diagrams) for reference solution over 30 years. (a) SST anomaly (K); (b) wind–stress anomaly τ (dyne cm^{-2}); (c) Kelvin wave amplitude q_0; and (d) first Rossby wave amplitude q_2. q_0 and q_2 are in nondimensional units.

Figure 3. Model–error correlations (based on $\mathbf{Q}$) projected from the wind–stress error: a) SST—SST; b) SST—q_0; c) SST–q_2; d) q_0–q_0; e) q_0–q_2; f) q_0–q_{14}; g) q_2–q_2; h) q_2–q_4; and i) q_2–q_{14} along the equator. The contour interval is 0.2.

Figure 4. RMS errors of LKF estimates for uncoupled case: a) SST anomaly; b) q_0; c) q_2.

Figure 5. Forecast–error correlations estimated by LKF based on $\mathbf{P}^{\mathrm{f}}$ for the uncoupled case at the end of year 5; same layout as in Fig. 3.

Figure 6. RMS errors of LKF estimates for the coupled case. Same layout as in Fig. 4.

Figure 7. Forecast–error correlations estimated by LKF based on $\mathbf{P}^{\mathrm{f}}$ for the coupled case; same layout as in Fig. 3. The correlations are calculated at the end of 5 years.

Figure 8. Simulated true state for 30 years: (a) SST anomaly (K); (b) wind–stress anomaly τ (dyne cm^{-2}); (c) Kelvin wave amplitude q_0; and (d) first Rossby wave amplitude q_2. q_0 and q_2 are in nondimensional unit.

Figure 9. Data assimilation with SST observation at 108W, indicated by the triangle. (a) SST anomaly; (b) diagonal components of $\mathbf{P}^{\mathrm{f}}$ (dashed) and $\mathbf{P}^{\mathrm{a}}$ (solid) for SST; (c) Kelvin wave amplitude q_0; and (d) $\mathbf{P}^{\mathrm{f}}$ (dashed) and $\mathbf{P}^{\mathrm{a}}$ (solid) for q_0.

Figure 10. Zonal variations of 30–year averaged RMS errors for the model forecast (short dashed line) and the assimilation with SST data at 152°E (SST_4: long dashed line), 177°E (SST_9: light solid line), and 108°W (SST_{20}: heavy solid line): (a) SST anomaly; (b) Kelvin wave amplitude q_0; (c) first Rossby wave amplitude q_2; and (d) second Rossby wave amplitude q_4. The errors are normalized by the maximum value of all the errors. The three observing locations are shown by filled triangles along the abscissa in each panel.

Figure 11. Same as in Figure 9, except that the assimilation is run with q_n observations at 111°W for 30 years.

Figure 12. Forecast–error correlations estimated by EKF at the end of 10–year assimilation with q_n data at 111°W. Same layout as in Fig. 3.

Figure 13. Same as in Figure 10, except that the assimilation is run with q_n observations for 30 years, at 149°E (q_{n4}: long dashed line)), 180°(q_{n9}: thin solid line), 111°W (q_{n20}: thick solid line). The three observing locations are shown by filled triangles along the abscissa.

Figure 14. Snapshots of weights assigned by the EKF to the data in the 2-q_n cases: q_{n4} (gray) and q_{n20} (black), plotted over 30 years at one-year intervals. Left panels are for the q_0 observations, right panels for the q_2 observations. The analysis fields are SST (top), q_0 (middle), and q_2 (bottom panel). The arrows in panel (d) denote the approximate locations of the peak weights during cold and warm phases. The two observing locations are shown by filled triangles (gray for the western and black for the eastern basin) in each panel.

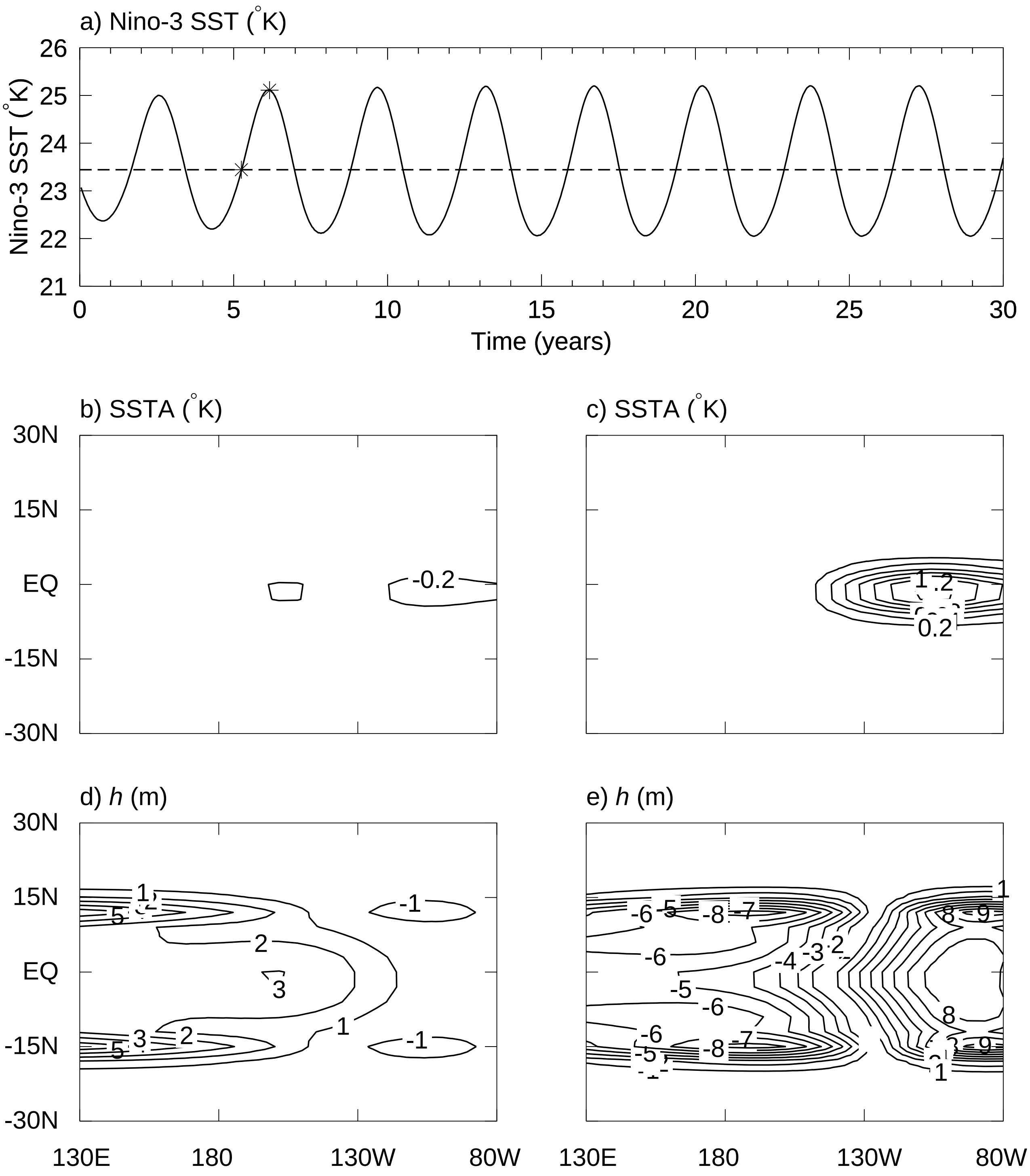
a) Nino-3 SST (°K)
Nino-3 SST (°K)
Time (years)
b) SSTA (°K)
c) SSTA (°K)
d) h (m)
e) h (m)
30N
15N
EQ
-15N
-30N
130E
180
130W
80W

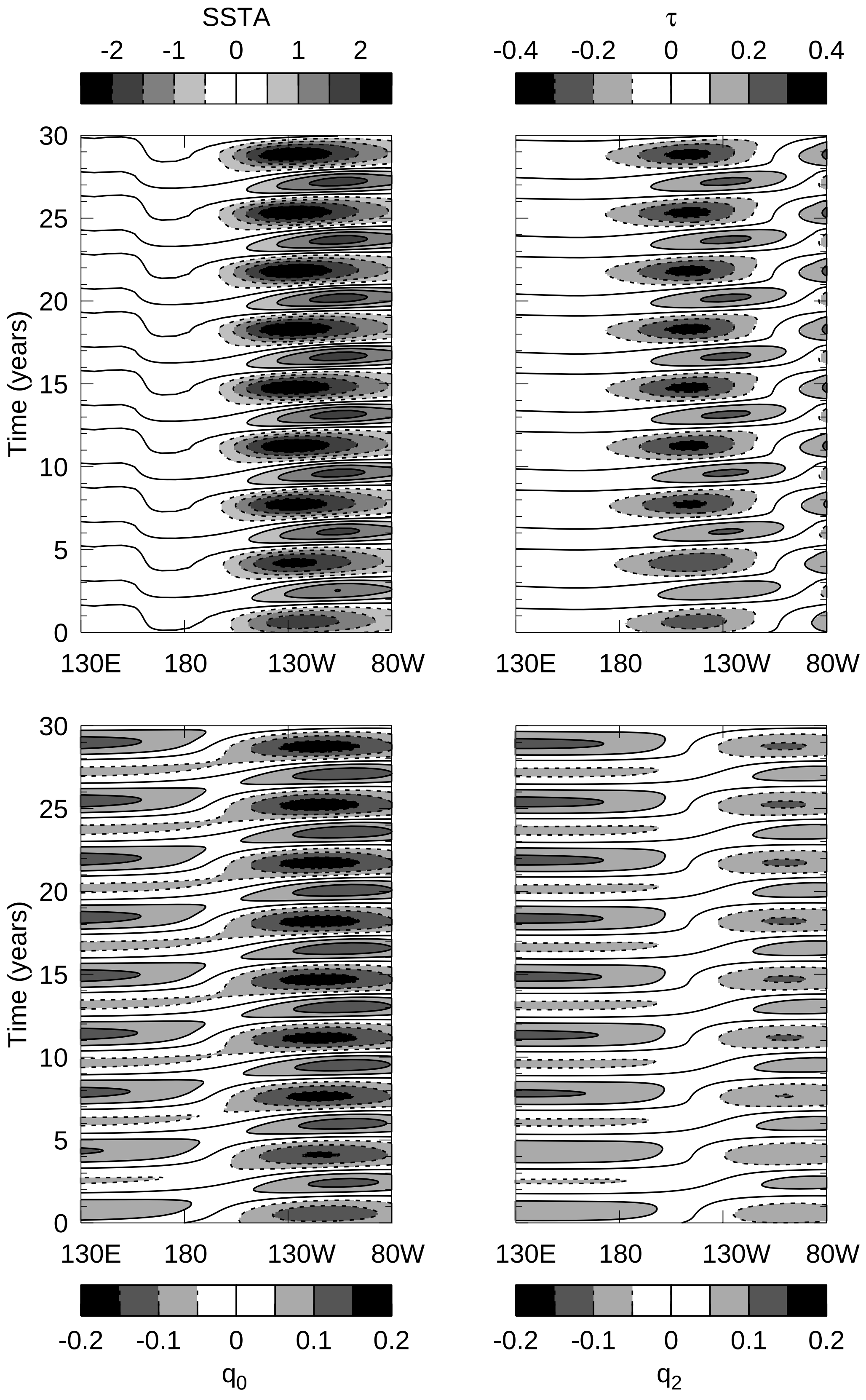
SSTA
-2 -1 0 1 2
τ
-0.4 -0.2 0 0.2 0.4
Time (years)
0 5 10 15 20 25 30
130E 180 130W 80W
-0.2 -0.1 0 0.1 0.2
q0
q2

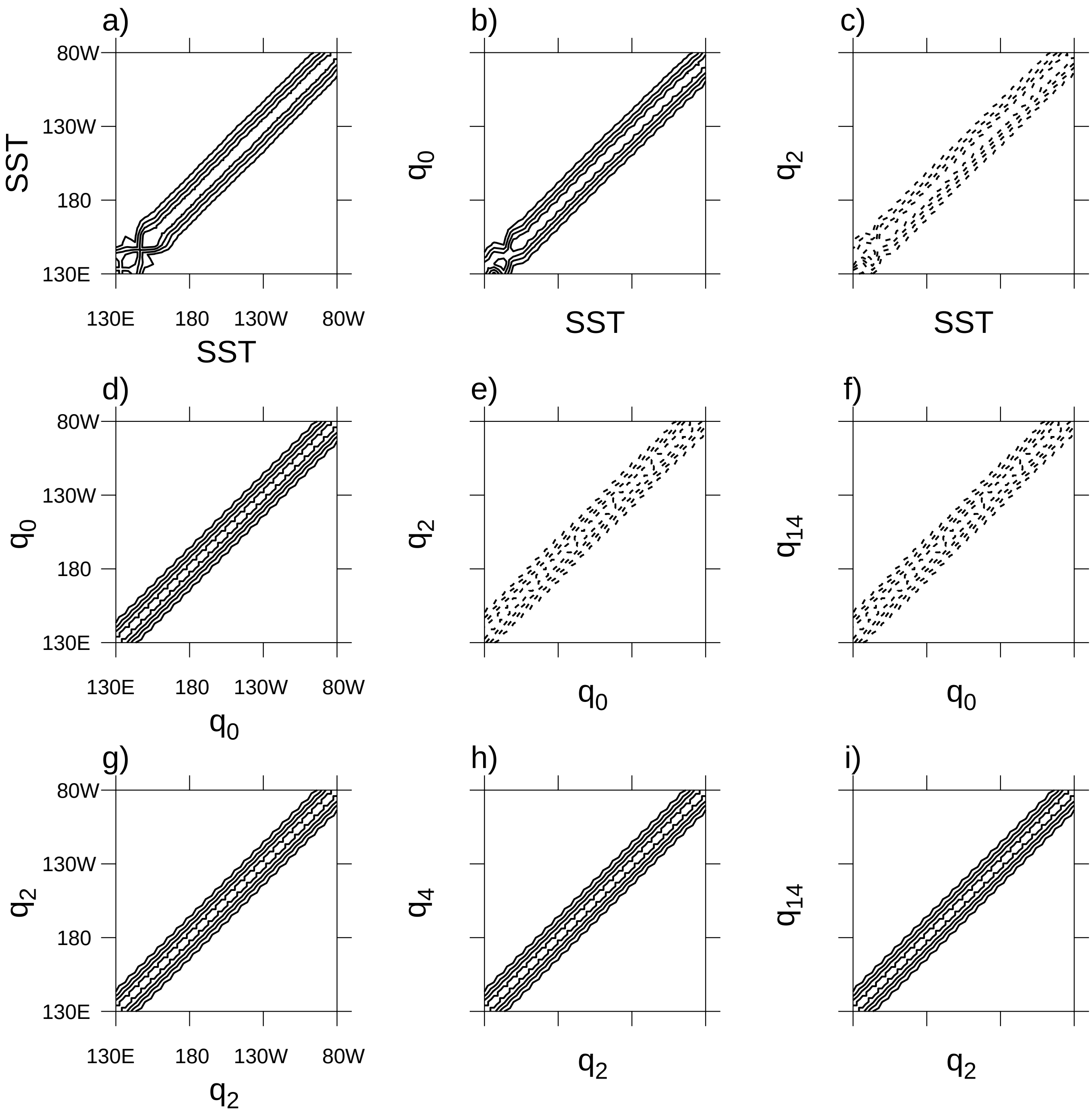
a)
b)
c)
d)
e)
f)
g)
h)
i)
80W
130W
180
130E
130E 180 130W 80W
SST
SST
q_0
q_2
SST
SST
q_0
q_2
q_{14}
q_0
q_0
q_0
q_2
q_4
q_{14}
q_2
q_2
q_2

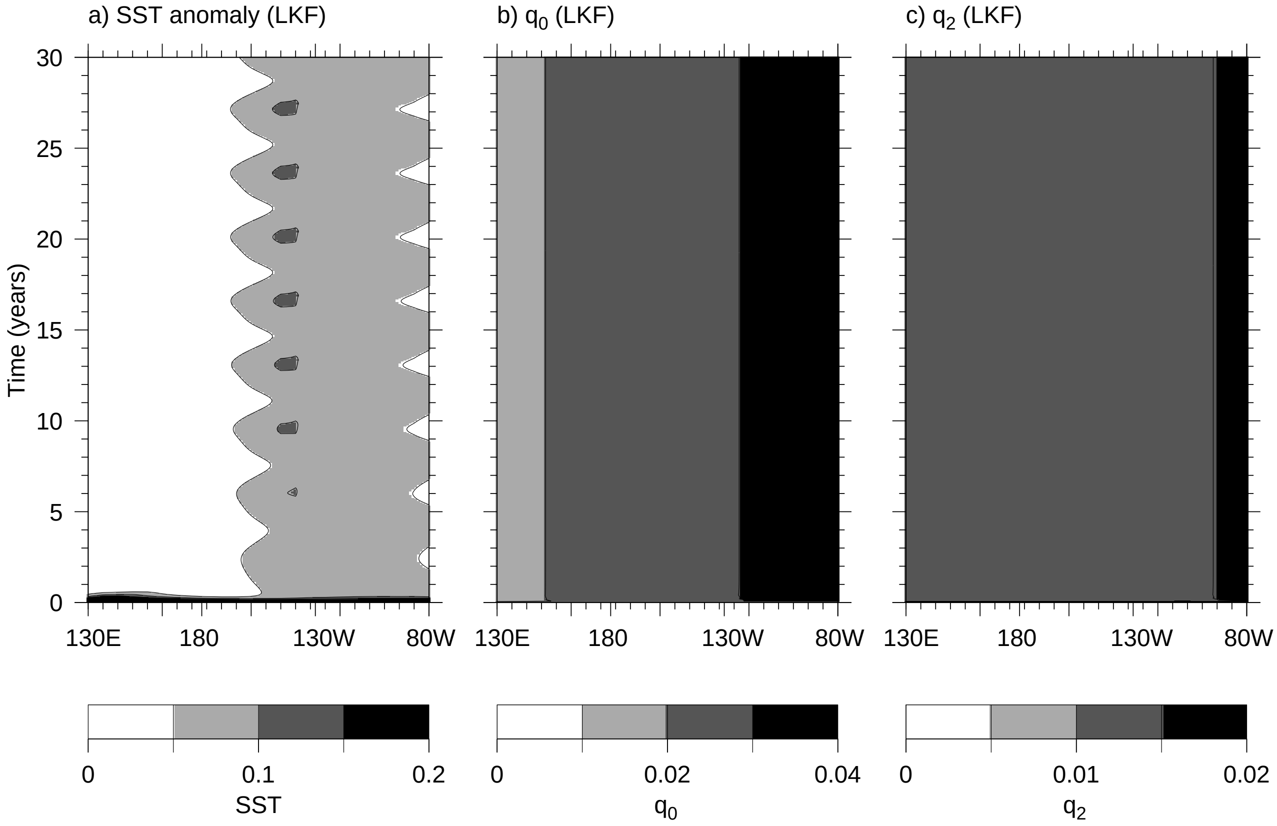
a) SST anomaly (LKF)
b) q_0 (LKF)
c) q_2 (LKF)
Time (years)
0
5
10
15
20
25
30
130E
180
130W
80W
0
0.1
0.2
SST
0
0.02
0.04
q_0
0
0.01
0.02
q_2

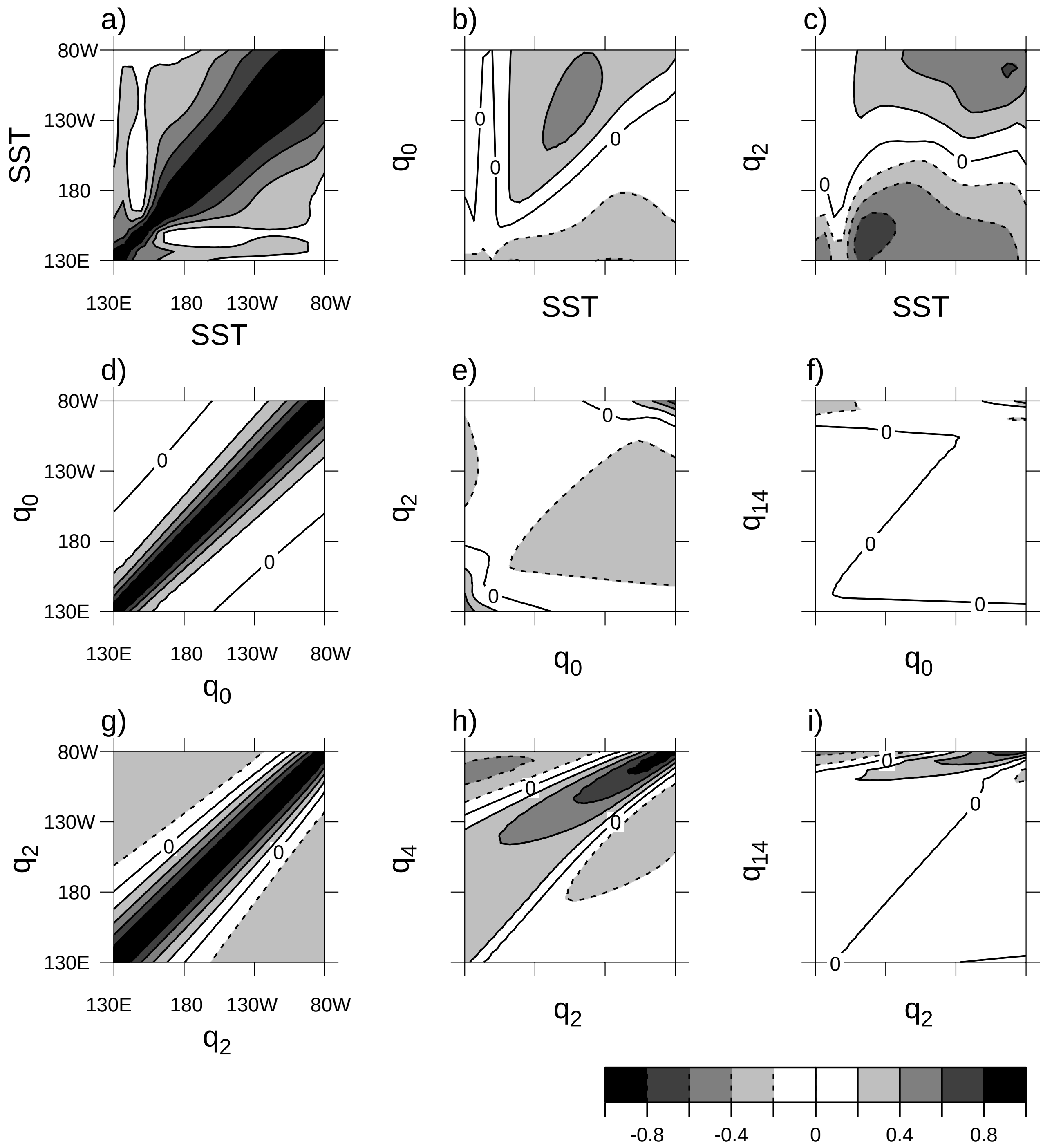
a)
b)
c)
80W
130W
180
130E
SST
130E 180 130W 80W
SST
q0
SST
q2
SST
d)
e)
f)
q0
q0
q2
q0
q14
q0
g)
h)
i)
q2
q2
q4
q2
q14
q2
0
-0.8
-0.4
0
0.4
0.8

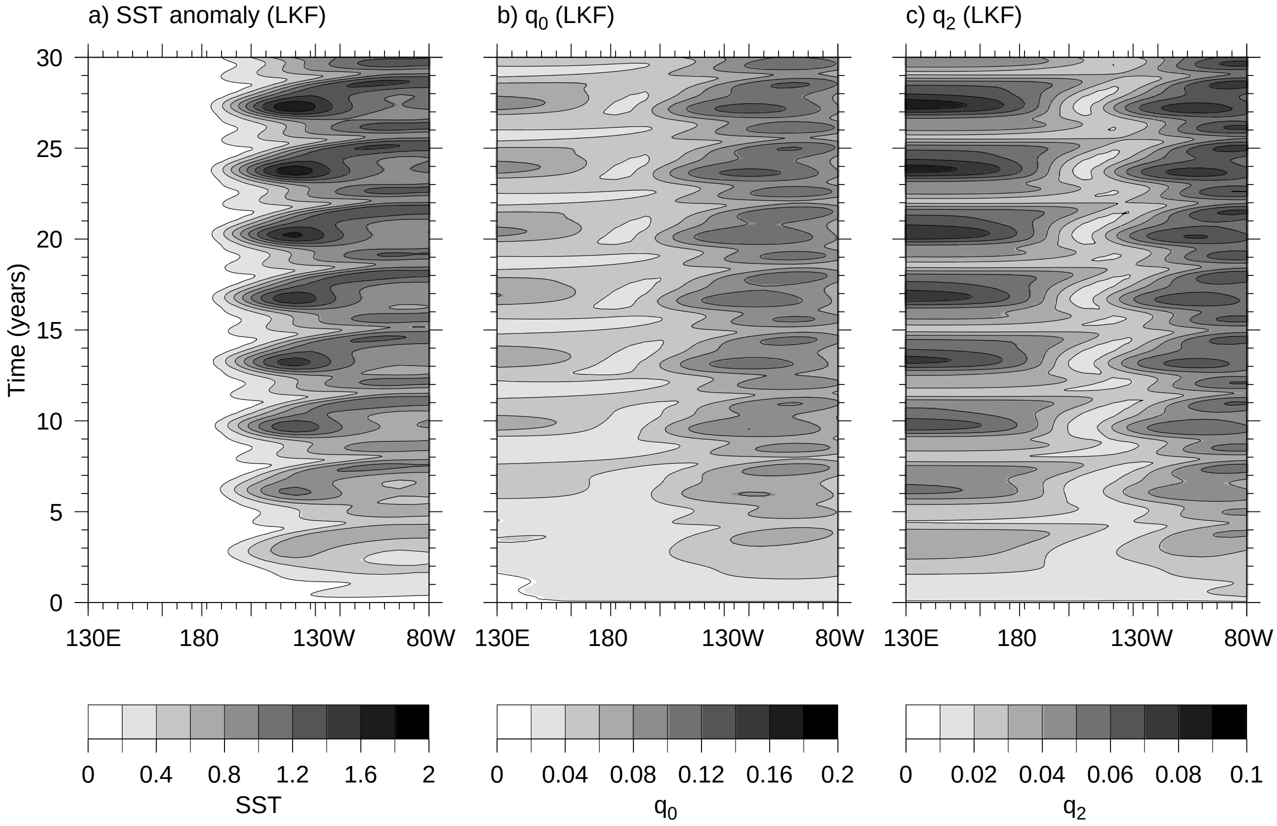
a) SST anomaly (LKF)
b) q_0 (LKF)
c) q_2 (LKF)
Time (years)
0
5
10
15
20
25
30
130E
180
130W
80W
0
0.4
0.8
1.2
1.6
2
SST
0
0.04
0.08
0.12
0.16
0.2
q_0
0
0.02
0.04
0.06
0.08
0.1
q_2

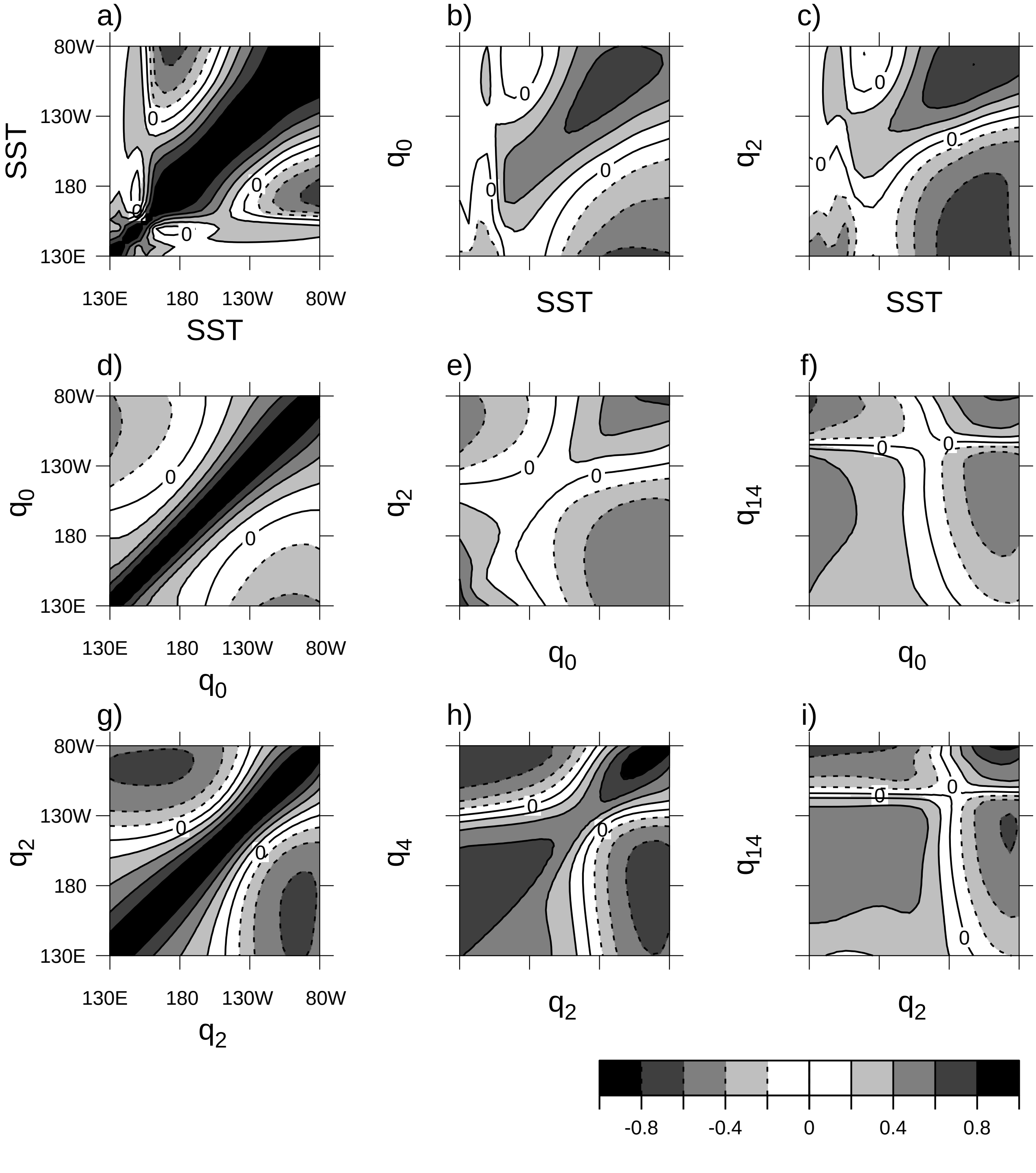
a)
b)
c)
d)
e)
f)
g)
h)
i)
80W
130W
180
130E
130E
180
130W
80W
SST
SST
SST
SST
q_0
q_2
q_0
q_2
q_{14}
q_0
q_0
q_0
q_2
q_4
q_{14}
q_2
q_2
q_2
0
-0.8
-0.4
0
0.4
0.8

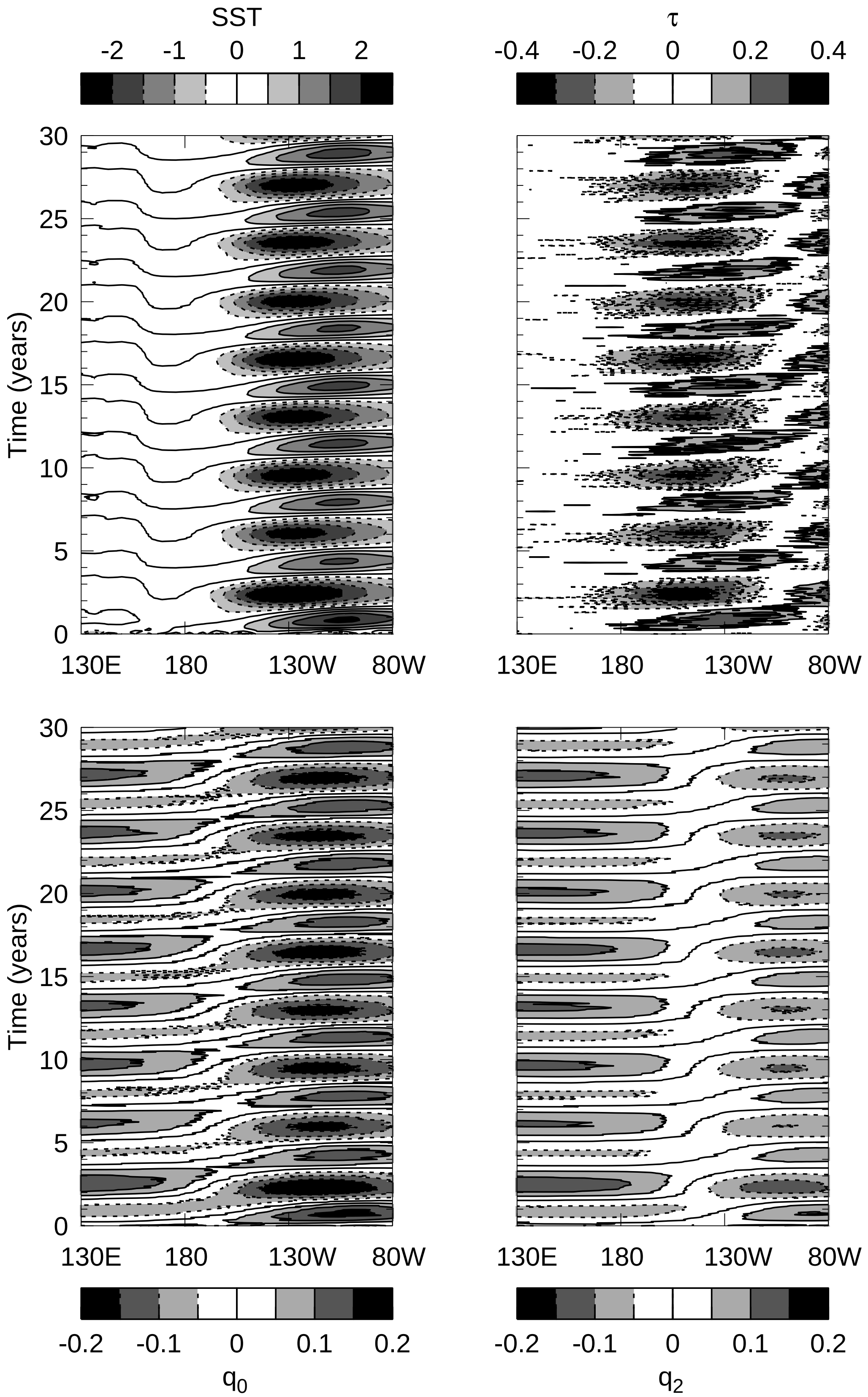
SST
-2 -1 0 1 2
τ
-0.4 -0.2 0 0.2 0.4
Time (years)
0 5 10 15 20 25 30
130E 180 130W 80W
-0.2 -0.1 0 0.1 0.2
q_0
q_2

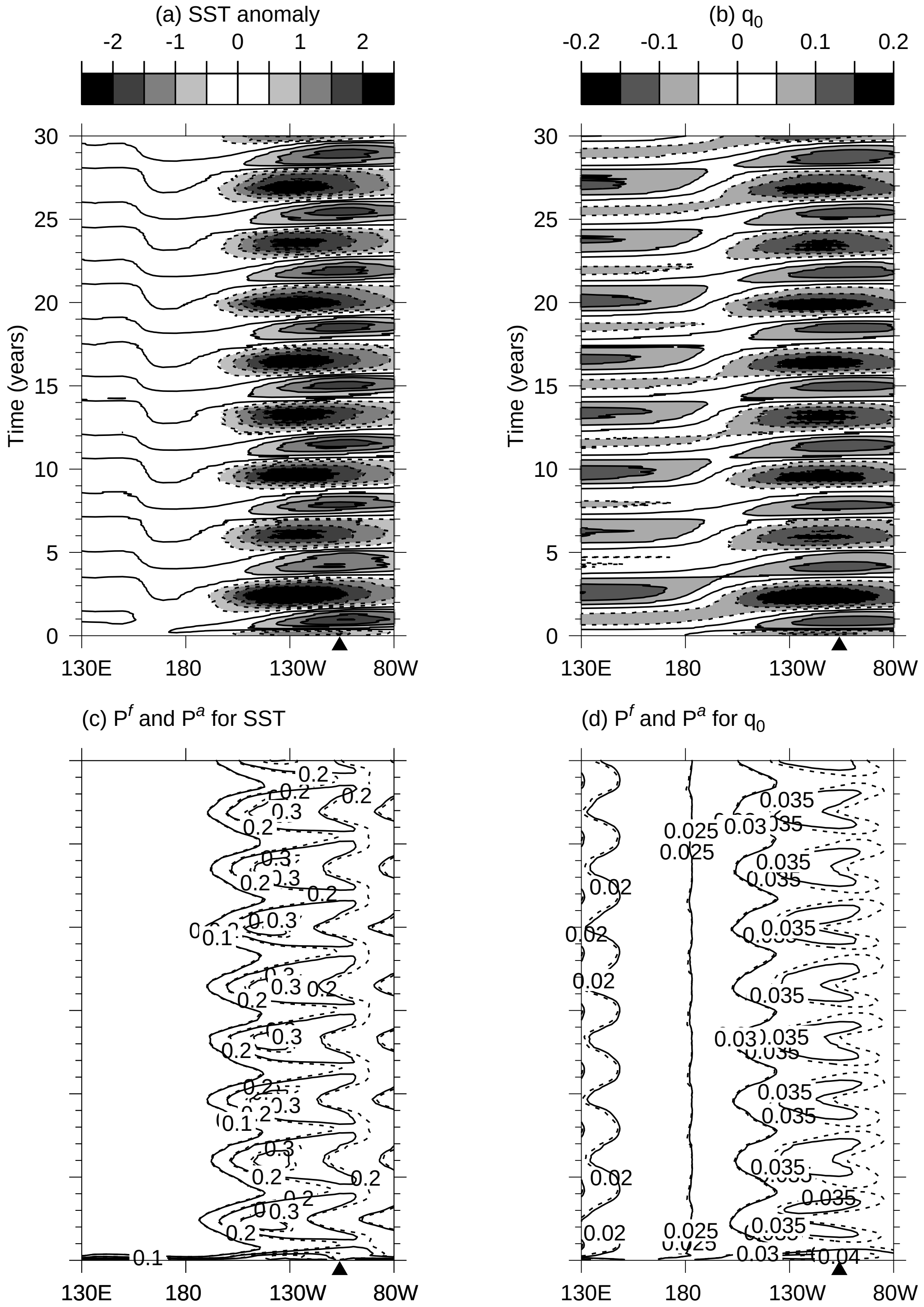
(a) SST anomaly
-2
-1
0
1
2
Time (years)
130E
180
130W
80W
(b) q_0
-0.2
-0.1
0
0.1
0.2
(c) P^f and P^a for SST
0.1
0.2
0.3
(d) P^f and P^a for q_0
0.02
0.025
0.03
0.035
0.04

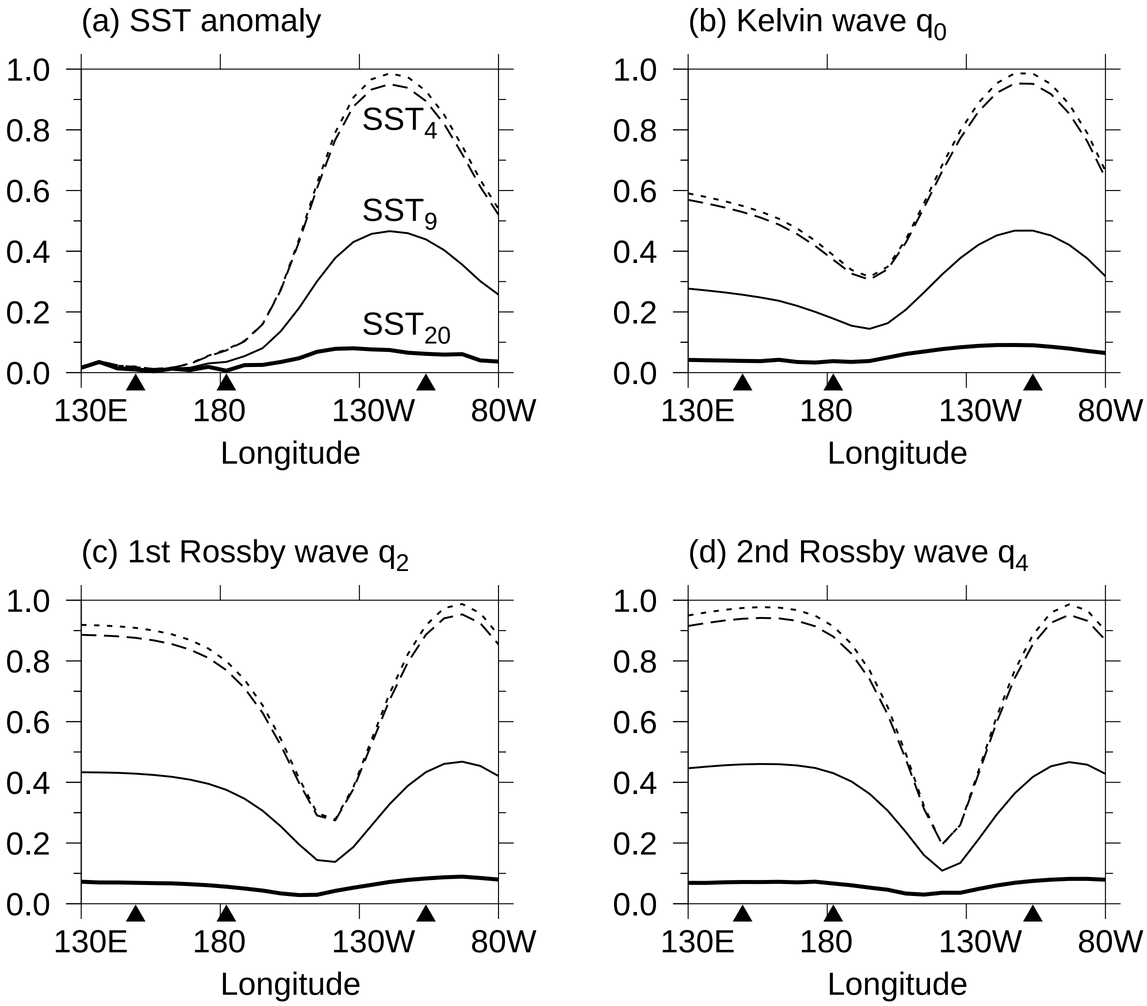
(a) SST anomaly
SST4
SST9
SST20
(b) Kelvin wave q0
(c) 1st Rossby wave q2
(d) 2nd Rossby wave q4
1.0
0.8
0.6
0.4
0.2
0.0
130E
180
130W
80W
Longitude

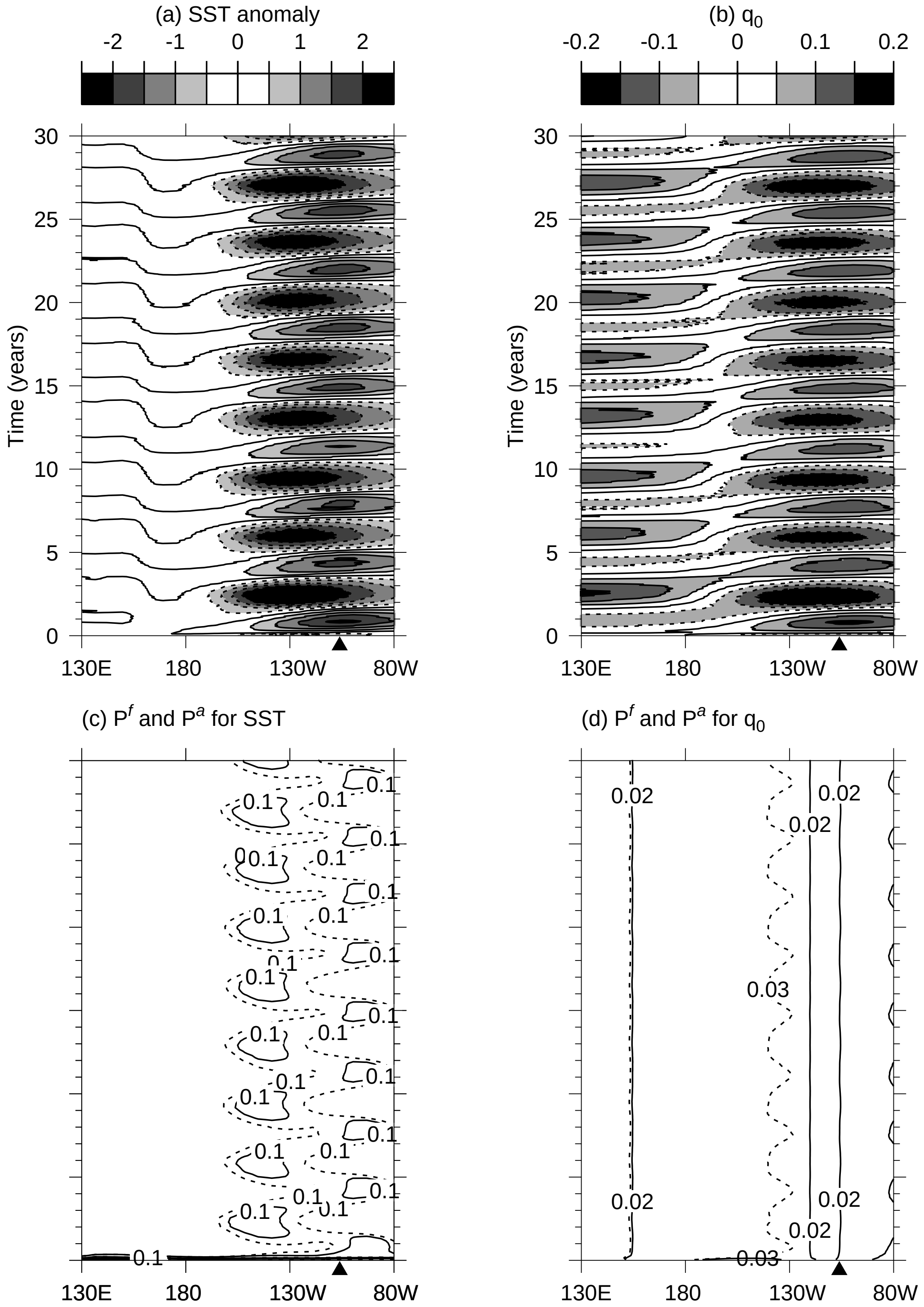

(a) SST anomaly
-2 -1 0 1 2
Time (years)
130E 180 130W 80W
(b) q_0
-0.2 -0.1 0 0.1 0.2
(c) P^f and P^a for SST
0.1
(d) P^f and P^a for q_0
0.02
0.03

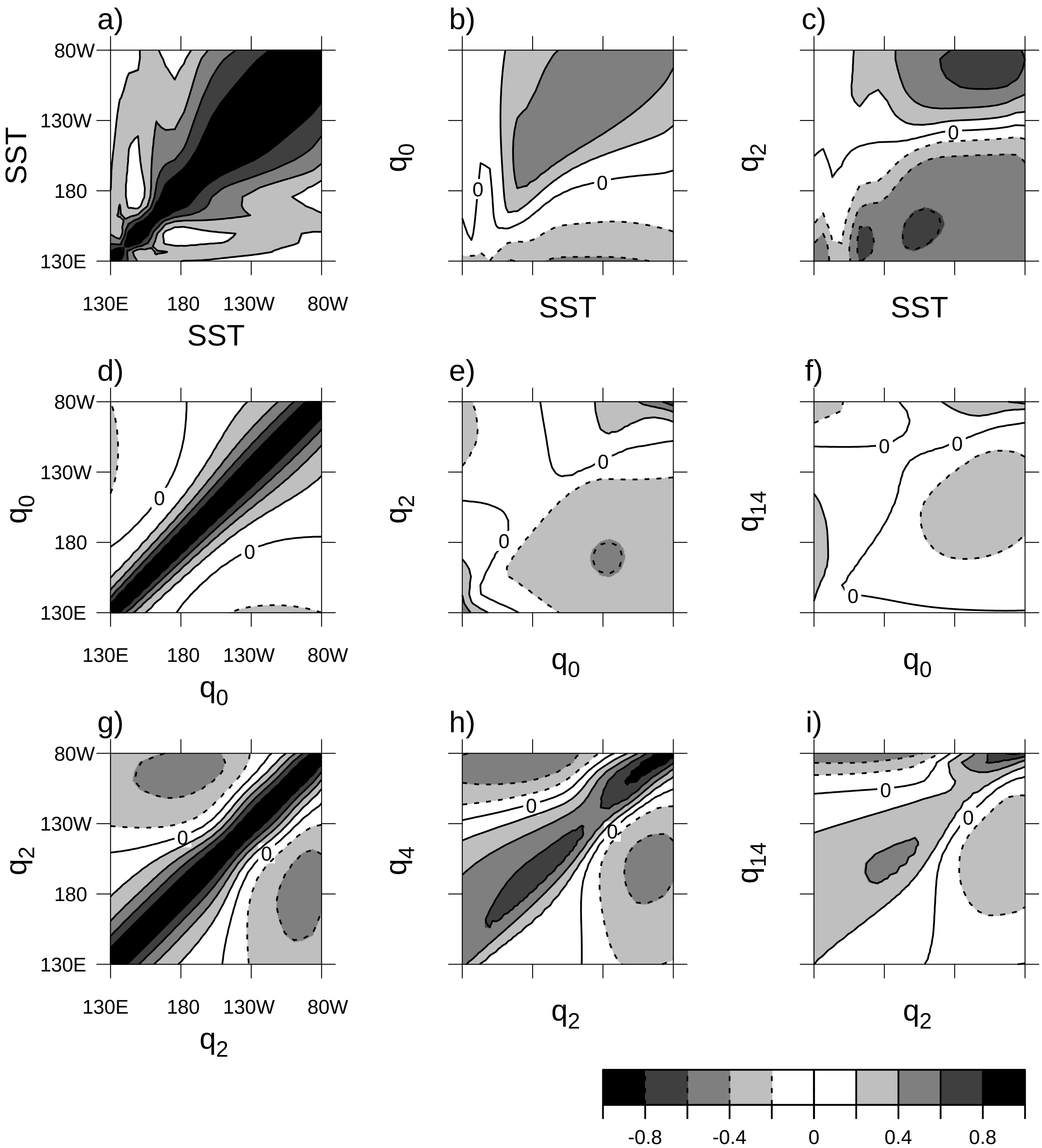
a)
b)
c)
SST
SST
q_0
q_2
SST
SST
0
0
0
80W
130W
180
130E
130E
180
130W
80W
d)
e)
f)
q_0
q_2
q_{14}
q_0
q_0
q_0
0
0
0
0
0
0
g)
h)
i)
q_2
q_4
q_{14}
q_2
q_2
q_2
0
0
0
0
0
0
-0.8
-0.4
0
0.4
0.8

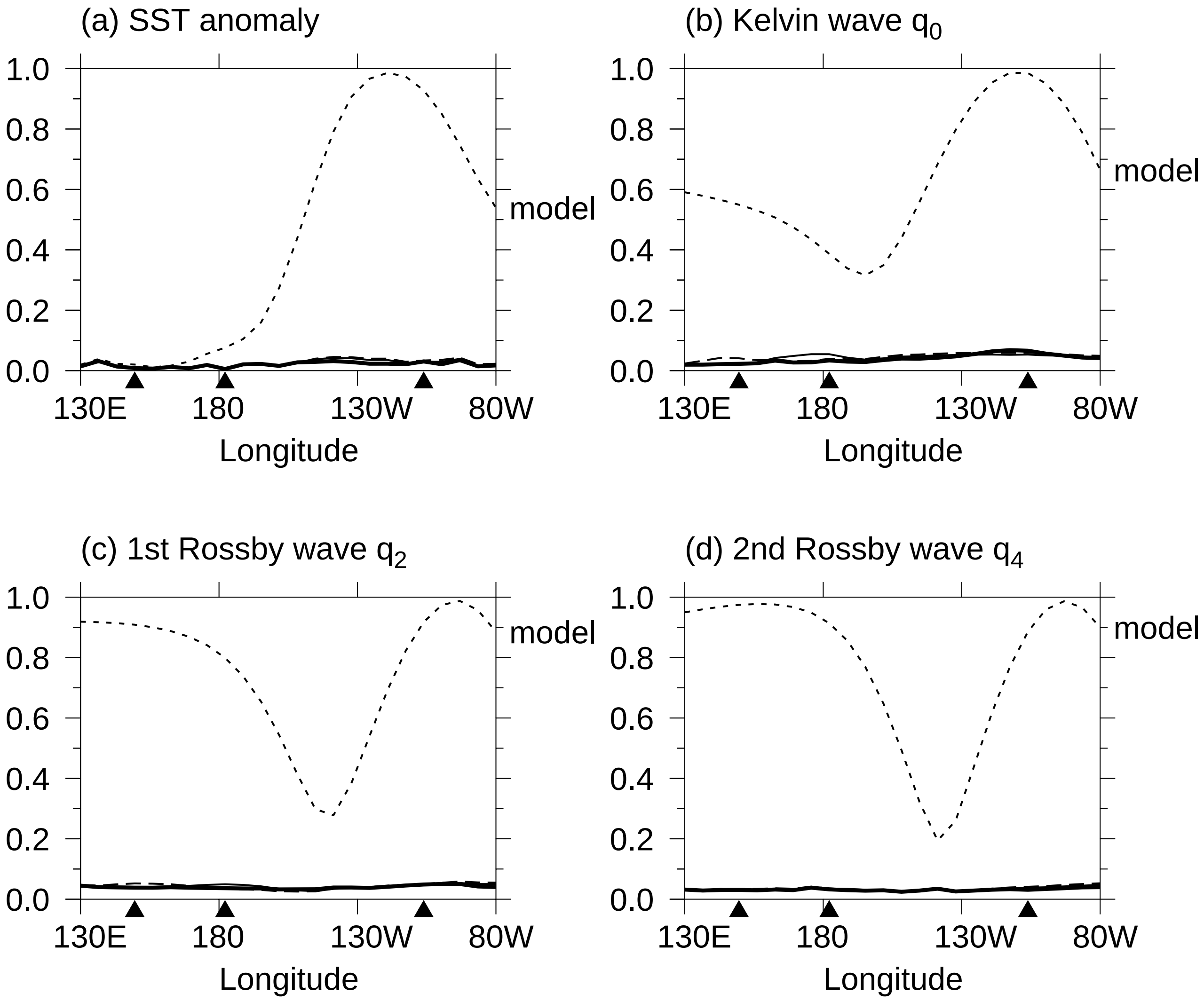
(a) SST anomaly
1.0
0.8
0.6
0.4
0.2
0.0
model
130E
180
130W
80W
Longitude
(b) Kelvin wave q_0
1.0
0.8
0.6
0.4
0.2
0.0
model
130E
180
130W
80W
Longitude
(c) 1st Rossby wave q_2
1.0
0.8
0.6
0.4
0.2
0.0
model
130E
180
130W
80W
Longitude
(d) 2nd Rossby wave q_4
1.0
0.8
0.6
0.4
0.2
0.0
model
130E
180
130W
80W
Longitude

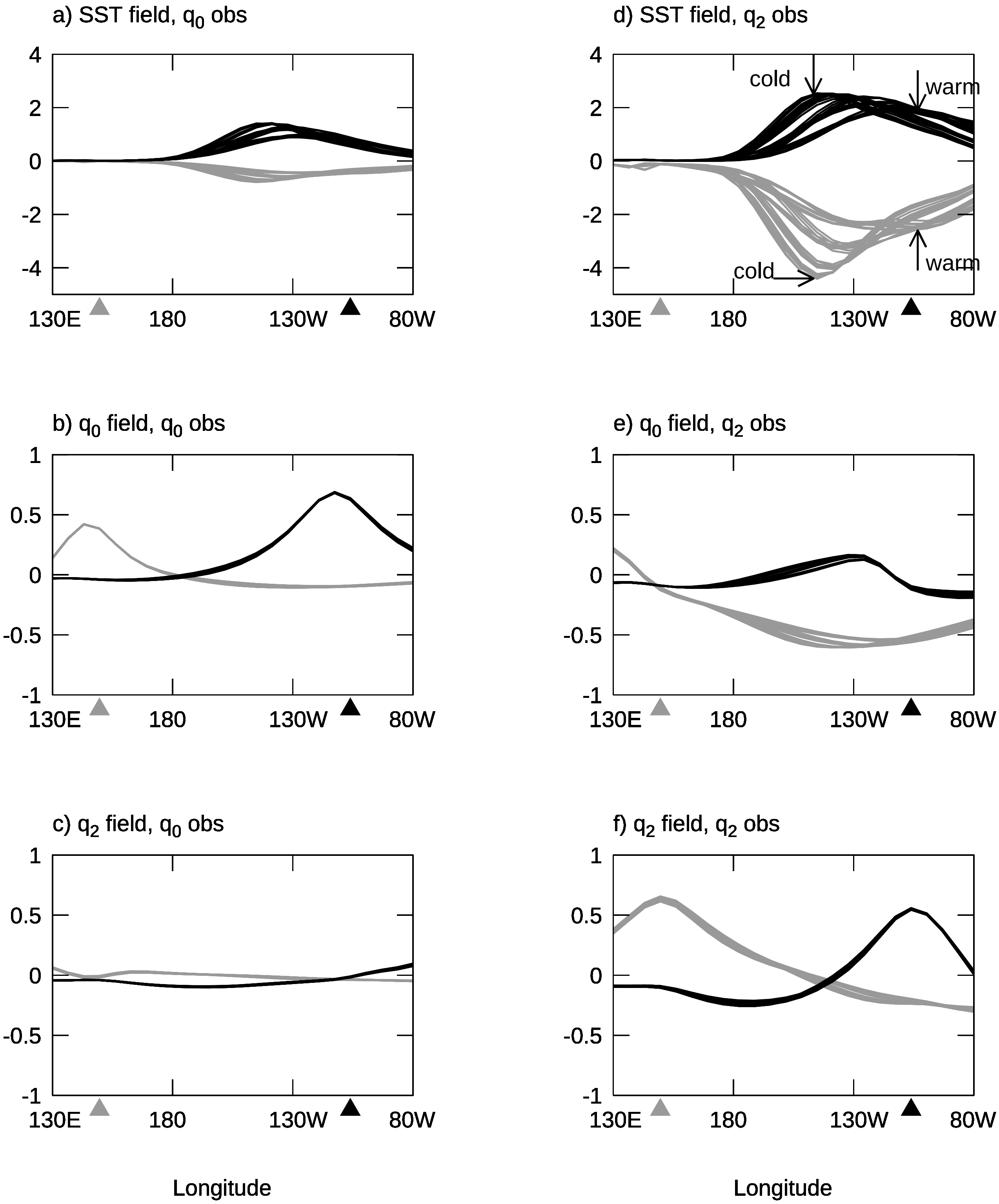
a) SST field, q_0 obs
b) q_0 field, q_0 obs
c) q_2 field, q_0 obs
d) SST field, q_2 obs
e) q_0 field, q_2 obs
f) q_2 field, q_2 obs
cold
warm
130E
180
130W
80W
Longitude

Table 1. Parameter values in the coupled ocean–atmosphere model

Parameters	Symbol	Values
Subsurface parameters		
Mean depth of the mixed layer	H_1	50 m
Mean depth of the thermocline layer	H_2	100 m
Mean depth of the active layer	H	150 m
Sensitivity parameter in T_{sub}	H_*	30 m
Offset parameter in T_{sub}	h_o	25 m
Effective depth of the upwelling	$H_{1.5}$	75 m
Temperature parameters		
Reference temperature	T_o	28°C
Off–equatorial SST	T_N	29°C
Temperature at thermocline	T_{so}	20°C
Damping coefficients		
Damping time for SST	ϵ_T^{-1}	90 days
Damping time for vertical mean current	ϵ^{-1}	2.5 years
Damping time for vertical shear current	ϵ_s^{-1}	2 days

Table 1. (continued)

Parameters	Symbol	Values
Coupling coefficients		
Relative coupling coefficient	μ	0.76
Surface-layer coefficient	δ_s	0.0
Other coefficients		
Relative adjustment time coefficient	δ	0.3
Longitudinal basin width	L_1	150°
Rayleigh friction coefficient	ϵ_a^{-1}	7500 km
time step	Δt	6 hours

Table 2. Comparison of forecast run and assimilation runs

Experiments	Niño-3 SST	q_0	q_2	q_4
No data assimilation	2.197	0.1342	0.0967	0.0850
EKF with SST_4 (152°E)	2.119	0.1297	0.0934	0.0821
EKF with SST_9 (177°W)	1.042	0.0632	0.0457	0.0403
EKF with SST_{15} (139°W)	0.222	0.0151	0.0102	0.0088
EKF with SST_{20} (108°W)	0.155	0.0126	0.0081	0.0068
EKF with 3$*$SST	0.132	0.0109	0.0069	0.0058
EKF with q_{n4} (149°E)	0.088	0.0098	0.0056	0.0039
EKF with q_{n9} (180°)	0.075	0.0091	0.0055	0.0037
EKF with q_{n20} (111°W)	0.063	0.0083	0.0051	0.0035
EKF with $2*q_n$	0.060	0.0091	0.0052	0.0033
EKF with $5*q_n$	0.055	0.0103	0.0051	0.0029

Thirty-year averaged RMS errors for forecast run (no data assimilation) or for assimilation runs with various data sets (see text for details) using the extended Kalman filter (EKF).